

Effects of the Geometry of the Line-Forming Region on the Properties of Cyclotron Resonant Scattering Lines

Michael Isenberg and D. Q. Lamb

Department of Astronomy and Astrophysics, University of Chicago, 5640 South Ellis
Avenue, Chicago, IL 60637

John C. L. Wang

Department of Astronomy, University of Maryland, College Park, MD 20742-2421

Received _____; accepted _____

Submitted to the *Astrophysical Journal*, 6 March 1997

ABSTRACT

We use a Monte Carlo radiative transfer code to examine the dependence of the properties of cyclotron resonant scattering lines on the spatial geometry and the optical depth of the line-forming region. We focus most of our attention on a line-forming region that is a plane-parallel slab. We also consider a cylindrical line-forming region. In both cases, the line-forming region contains an electron-proton plasma at the equilibrium Compton temperature, T_c , and is threaded with a uniform magnetic field with strength $\sim 10^{12}$ gauss. We consider geometries in which the photon source illuminates the line-forming region from below, and in which the photon source is embedded in the line-forming region. The former may correspond to a line-forming region in the magnetosphere of a neutron star, illuminated from below; the latter to a line-forming region on or near the surface of a neutron star as in an accretion column.

In the case of the plane-parallel slab line-forming region, we study the behavior of the resonant Compton temperature and the properties of the cyclotron scattering lines as a function of the column depth of the line-forming region and the orientation of the magnetic field. At small or moderate optical depths ($N_e \ll 10^{25} \text{ cm}^{-2}$ [electron scattering optical depth $\tau_{T_o} \ll 10$]), the resonant Compton temperature ranges from $T_e/E_B \approx 0.2$ when the magnetic field is perpendicular to the slab to $T_e/E_B \approx 0.4$ when the field is parallel to the slab. At large optical depths ($N_e \gtrsim 1.5 \times 10^{25} \text{ cm}^{-2}$ [$\tau_{T_o} \gtrsim 10$]), the resonant Compton temperature is higher.

At small or moderate optical depths ($\tau_{T_o} \ll 10$), the equivalent widths, W_E , of the spectral lines depend on two effects. First, W_E increases as the viewing angle *with respect to the field* decreases, due to Doppler broadening. Second, W_E increases as the viewing angle *with respect to the slab normal*

increases, due to the increase in column depth along the line of sight. When the magnetic field is parallel to the slab and the viewing angle is along the field, for example, both effects are large; in a line-forming region whose optical depth is moderate, the first harmonic equivalent width can reach $\sim 0.75E_B$. Shoulders are present on each side of the first harmonic line when the spectrum is viewed at angles with respect to the slab normal corresponding to $\mu_{sl} = \cos\theta_{sl} \gtrsim 0.25$ ($\theta_{sl} \lesssim 75^\circ$), and become stronger with increasing column depth, until column depths $N_e \lesssim 1.5 \times 10^{25} \text{cm}^{-2}$. As a result, the W_E of the first harmonic reaches a maximum value, and then decreases with increasing column depth (optical depth) in the line-forming region. The shoulders are the result of injecting the photon spectrum at moderate optical depths. When the photon spectrum is injected at sufficiently large optical depths ($\tau_{To} \gtrsim 10$), continuum scattering smears the shoulders so that they are no longer visible and the equivalent width of the first harmonic resumes increasing with increasing column depth.

In the case of the cylindrical line-forming region, we consider only a magnetic field oriented along the axis of the cylinder. This corresponds to the situation expected in the canonical model of the emission region of accretion-powered pulsars. We find that the emerging spectrum is similar to that of the slab line-forming region with an embedded photon source and the magnetic field perpendicular to the slab normal. Thus, at large optical depths we expect the cyclotron line from a cylindrical line-forming region to have a very large equivalent width W_E , nearly independent of viewing angle, and no visible shoulders.

Our findings have implications for accretion-powered pulsars and gamma-ray bursters. In particular, the absence of pronounced shoulders on each side of the cyclotron first harmonic line in the spectra of accretion-powered pulsars suggests

that the line-forming region is either illuminated from below and outside, as would be the case if it were plasma suspended in the magnetosphere of the neutron star, or it has a large ($\tau_{T_o} \gtrsim 10$) optical depth. Also, the ability of a slab line-forming region in which the magnetic field is parallel to the slab to produce narrow lines with large W_E suggests that the lines observed in the X-ray spectra of some gamma-ray bursts might be able to be formed in plasma trapped at the magnetic equator of a neutron star.

1. Introduction

Cyclotron lines in an astrophysical x-ray spectrum are the clear signature of a superstrong magnetic field in the line-forming region. Consequently, they are an important clue to the nature of the source and the properties of the emission region, especially at energies $\gtrsim 10$ keV where atomic lines are not available. Cyclotron lines have been important in identifying accreting magnetized neutron stars as the source of radiation in about a dozen X-ray pulsars (Mihara 1995; Makishima and Mihara 1992), including Her X-1 (Trümper *et al.* 1978), 4U 0115+63 (Wheaton *et al.* 1979), 4U 1538-52 (Clark *et al.* 1990), and A0535+26 (Grove *et al.* 1995). Absorption-like features have also been observed in classical gamma-ray bursts and interpreted as cyclotron lines (Mazets *et al.* 1980, 1981; Heuter 1984; Murakami *et al.* 1988; Fenimore *et al.* 1988; Harding and Preece 1989; Wang *et al.* 1989; Alexander and Mészáros 1989; Lamb *et al.* 1989; Yoshida *et al.* 1991; Nishimura and Ebisuzaki 1992; Nishimura 1994; Mazets *et al.* 1996; Briggs 1996). Although the observation of spectral features in gamma-ray bursts and their interpretation continue to be controversial, they are perhaps the strongest evidence that at least some gamma-ray bursts come from strongly magnetized neutron stars associated with our own galaxy.

By building theoretical models of line-forming regions and comparing the emerging spectra with observations, theorists have been able to infer *quantitatively* many properties of the sources that are believed to possess cyclotron lines. For example, Mészáros and Nagel (1985) use a Feautrier calculation to show that the spectrum of Her X-1 could be produced in a region with magnetic field $B_{12} \equiv B/(10^{12}\text{gauss})=3.3$ oriented parallel to the normal of a slab atmosphere with column depth (slab width) $N_{e,21} \equiv N_e/(10^{21} \text{ electrons cm}^{-2}) = 10^4$ and electron temperature $T_e=7$ keV. Other fits to accretion-powered pulsar spectra include those of Araya and Harding (1996), who infer the presence of a magnetic field approaching the critical field, $B_{crit,12} = 44.14$ from the spectrum of A0535+26. For gamma-ray bursts,

Wang *et al.* (1989) use a Monte Carlo radiative transfer code (Wang, Wasserman, and Salpeter 1988; Lamb *et al.* 1989) to show that the cyclotron lines in the spectrum of the burst GB880205 could be produced in a region with $B_{12}=1.7$, $N_{e,21}=1.2$, and with electrons at the equilibrium Compton temperature, T_c , which is 5.3 keV in this case.

Wang *et al.* (1989) inject an initial photon distribution into a plane-parallel slab atmosphere from a source plane below the slab. Here we consider both this model and one in which the photons are injected at a source plane embedded inside the slab. A slab illuminated from below may correspond to a line-forming region in the magnetosphere of a neutron star (cf. Dermer and Sturmer 1991; Sturmer and Dermer 1994; see also Zheleznyakov and Serber 1994, 1995). A slab illuminated from within may correspond to a line forming region in a semi-infinite atmosphere at the stellar surface (see Slater, Salpeter, and Wasserman 1982; Wang, Wasserman, Salpeter 1988, 1989; Freeman *et al.* 1992; Nelson *et al.* 1997).

Wang *et al.* (1989) take the magnetic field to be oriented along the slab normal, \hat{z}_{sl} (i.e. $\Psi = 0$). Such fields are found near the magnetic poles of neutron stars with dipole fields. Kaminker, Pavlov and Shibano (1982, 1983) and Burnard, Arons, and Klein (1991) consider the effects of varying the angle Ψ between the magnetic field and the slab normal. However, these authors do not include the effects of scattering in the cyclotron line core (see Section 3); Burnard, Arons, and Klein (1991) calculate the spectrum in the continuum only, while Kaminker, Pavlov, and Shibano’s (1982, 1983) calculation is valid for the continuum and the line wings.

In the present work, we consider scattering in line-forming regions with $\Psi \neq 0$, *including* core scattering. Fields at angles other than $\Psi = 0$ occur when lines are formed in structures near the magnetic poles, such as accretion columns or mounds (Burnard, Arons, and Klein 1991). Line-forming regions with $\Psi \neq 0$ also correspond to non-polar regions on

the surface or in the magnetosphere of neutron stars with dipole fields, as well as regions on stars with more complicated fields. For example, the surface of a neutron star may be threaded by local fields with various orientations relative to the local slab normal, instead of or in addition to a global dipole field (see, e.g., Ruderman 1991a,b,c; Lamb, Miller, and Taam 1996).

We will show that if the magnetic field is oriented perpendicular to the slab normal ($\Psi = \pi/2$) and the photon source is embedded in the slab, the line properties are similar to those for a cylindrical line-forming region. Thus a slab line-forming region with this geometry is a good approximation to the cylindrical line-forming region expected in the canonical model of accretion-powered pulsars.

In Section 2 we discuss the geometry of the line-forming regions we use in our calculations. In Section 3 we describe the Monte Carlo radiative transfer code. We show how the equilibrium Compton temperature varies with the field orientation in Section 4. In Section 5 we present the spectra calculated by the Monte Carlo code and discuss the effects of the line-forming region geometry on the properties of the emergent lines. Finally, in Section 6 we discuss the implications of our calculations for accretion-powered pulsars and gamma-ray bursters.

2. Spatial Geometry of the Line-Forming Region

2.1. Slab Geometry

The principal spatial geometry we study in this paper, a plane parallel slab, is shown in Figure 1a. Photons are injected at the source plane, travel through an electron-proton plasma, and emerge from one or the other of the faces of the slab. The horizontal extent of the slab is infinite. The angle θ is the polar angle of a photon’s direction of propagation

with respect to the magnetic field. The polar angle is usually specified in terms of $\mu \equiv \cos \theta$. Similarly, θ_{sl} and φ_{sl} are the polar and azimuthal angles, respectively, of a photon *with respect to the slab normal* and $\mu_{sl} \equiv \cos \theta_{sl}$.

As the Figure shows, N_e is the column depth between the top of the slab and the source plane, while N'_e is the column depth between the source plane and the bottom of the slab. In some circumstances, we will also specify the column depth in terms of the Thomson depth, $\tau_{To} \equiv N_e \sigma_T$, where $\sigma_T \equiv (8\pi/3)(e^2/(m_e c^2))^2 = 6.65 \times 10^{-25} \text{ cm}^2$ is the Thomson cross section. We stress that in general the optical depth encountered by a given photon will differ from the Thomson depth since the actual scattering cross section varies with photon energy, direction, and polarization.

We characterize the position of the source plane by the ratio of N_e to N'_e . Thus, for a slab illuminated from below, as in Wang *et al.* (1989), the column depth between the source plane and the bottom of the slab is zero; we call this the 1-0 geometry. Similarly, a slab with the source plane embedded in the middle of the slab, so that $N_e = N'_e$, has a 1-1 geometry.

Slater, Salpeter, and Wasserman (1982) and Wang, Wasserman, and Salpeter (1988) determine that the mean number of scatters between the source and the top edge that a resonant photon experiences prior to escape approaches a limiting value as the atmosphere becomes semi-infinite (i.e. as $N'_e/N_e \rightarrow \infty$). It is generally within ten percent of its limiting value in the 1-1 geometry and indistinguishable from its limiting value in the 1-4 geometry. The corresponding mean path length the photon travels between the source and the top edge displays similar behavior, as does the median frequency shift of the escaping photon. Thus the 1-4 geometry is an excellent approximation to a semi-infinite atmosphere. Unfortunately, our Monte Carlo simulations show that the total number of scatters per injected photon in the 1-4 geometry is approximately three times the number of scatters

in the 1-1. The computer time required for the simulation increases proportionately. Consequently, we use the 1-1 geometry in the present work as a compromise between the quality of the approximation to a semi-infinite atmosphere and the amount of computer time required.

We refer to photons that emerge from the top of the slab as *transmitted* and those that emerge from the bottom as *reflected*. The former reach the observer. In the 1-0 geometry, we assume that the latter return to the stellar surface where they are thermalized, i.e., absorbed by nonresonant inverse magnetic bremsstrahlung. In the 1-1 geometry the reflection symmetry of the line-forming region across the source plane ensures that the transmitted and reflected spectra for isotropically injected photons are the same. We can, therefore, set the transmitted spectrum for isotropic injection equal to the *sum* of the transmitted and reflected spectra for *semi*-isotropic injection. By doing so, we can reduce the computer time required per transmitted photon by an additional factor ~ 2 in the 1-1 geometry as compared with the 1-4 geometry.

2.2. Cylindrical Geometry

We also consider a cylindrical geometry, as shown in Figure 1b. The length of the cylinder is infinite. We only consider magnetic fields oriented parallel to the cylinder axis, as expected in the canonical model of the emission region of accretion-powered pulsars. Photons are injected along the cylinder axis and emerge from the surface of the cylinder. As in the slab geometry, the angle θ is the polar angle of a photon's direction of propagation with respect to the magnetic field. The column depth between the cylinder axis and the surface of the cylinder is N_e .

3. Monte Carlo Radiative Transfer Code

Our Monte Carlo radiative transfer code is an extended version of that used by Wang *et al.* (1989). The code injects an initial photon distribution $N_i(E)$ into an isothermal, fully ionized slab atmosphere with a uniform magnetic field at an angle Ψ to the slab normal. It then follows each photon through the slab and determines the emergent spectrum.

The code uses resonant scattering cross sections that have been averaged over the initial polarization states and summed over the final states. Wang, Wasserman, and Salpeter (1988) argue that polarization averaged cross sections are appropriate for first harmonic scattering in optically thick media when the vacuum contribution to the dielectric tensor dominates the plasma contribution. This will be the case when

$$\frac{w}{\delta} = 0.04 \left(\frac{n_e}{10^{20} \text{ cm}^{-3}} \right) B_{12}^{-4} \ll 1, \quad (1)$$

where $w \equiv (\hbar\omega_p/E_B)^2$ is the plasma frequency parameter, ω_p is the plasma frequency, $E_B = 11.6 \text{ keV } B_{12}$ is the cyclotron energy, δ is the magnetic vacuum polarization parameter (see, e.g., Adler 1971), and n_e is the electron number density. This condition will generally hold under the physical conditions studied in this paper.

We work in the cold plasma approximation, in which $kT_e \ll E_B$. In this approximation, the Landau level spacing is much larger than the typical electron energy so the Landau levels are not collisionally populated. We further assume that the photon densities are sufficiently low so that the levels are not radiatively populated. Thus, in each scattering the initial and final electron state is the Landau ground state ($n = 0$). We denote scattering channels by the sequence of Landau levels that the electron occupies, e.g. $0 \rightarrow 0$, $0 \rightarrow 1 \rightarrow 0$, and $0 \rightarrow 3 \rightarrow 2 \rightarrow 0$.

In our treatment of electron-photon scattering, we adopt the approximation

$$\left| \sum_i a_i \right|^2 \approx |a_{0 \rightarrow 0} + a_{0 \rightarrow 1 \rightarrow 0}|^2 + \sum_{\substack{i \neq 0 \rightarrow 0, \\ 0 \rightarrow 1 \rightarrow 0}} |a_i|^2, \quad (2)$$

where a_i is the matrix element for the i^{th} scattering channel. In general, this approximation is a good one only near the line centers. Consequently, eq. (2) is valid for line-forming regions which are not optically thick in the line wings of the first harmonic (see below; also Wasserman & Salpeter 1980; Lamb *et al.* 1989), that is

$$\tau_1 \lesssim 1/a, \quad (3)$$

where

$$\tau_1 = 100 N_{e,21} B_{12}^{-1} \left(\frac{T_e}{1 \text{ keV}} \right)^{-1/2} \quad (4)$$

is the polarization-, angle-, and frequency-averaged optical depth in the first harmonic,

$$a \equiv \frac{\Gamma_1}{2E_d^1} = 1.8 \times 10^{-3} B_{12} \left(\frac{T_e}{1 \text{ keV}} \right)^{-1/2} \quad (5)$$

is the dimensionless natural line width,

$$E_d^n \equiv n E_B \sqrt{\frac{2T_e}{m_e c^2}} = 0.73 n B_{12} \left(\frac{T_e}{1 \text{ keV}} \right)^{1/2} \quad (6)$$

is the Doppler width associated with the n^{th} harmonic,

$$\Gamma_n = \frac{4n\alpha E_B^2}{3m_e c^2} = 2.6 \times 10^{-3} \text{ keV } n B_{12}^2 \quad (7)$$

is the radiative width for the n^{th} harmonic, and α is the fine structure constant. Even when the line-forming region is optically thick in the line wings, eq. (2) is still a good approximation if the spectrum has an exponential rollover such that there are very few photons beyond the first harmonic. This is usually the case for the spectra of accretion-powered pulsars (Mihara 1995). Thus, for instance, for rollover energies of $kT_\gamma \approx E_B/4$, the number of photons with energies significantly above the first harmonic is negligible. In this case only continuum and first harmonic scattering will be significant. However, if neither of these conditions hold, we cannot ignore the cross terms when squaring the matrix element, as we have in eq. (2). For the most part, in the present work, we confine ourselves to cases where eq. (2) is valid. However, we shall see below that when the magnetic field is parallel to the slab, photons traveling along the slab see a very large column depth *and* a large cross section and so can scatter multiple times with a wide range of electron velocities. Some of these photons can therefore continue to scatter far in the line wings above $\sim E_B$ where eq. (2) no longer holds. However, the range of magnetic field orientations and photon directions where this occurs is small.

The scattering cross section we use is valid in the limit $(E^r/m_e c^2)^2 b^{-1} \ll 1$, where $b \equiv B/B_{\text{crit}}$, E is the photon energy, and the superscript r denotes quantities measured in the frame of reference where the electron is at rest ($p_z = 0$) prior to scattering, that is, the pre-scattered electron's rest frame (see, e.g., Daugherty and Ventura 1977). This limit applies throughout the present work. For the $0 \rightarrow 0$ and $0 \rightarrow 1 \rightarrow 0$ channels, these limits give the classical magnetic Compton scattering cross section. When evaluated in the pre-scattered electron's rest frame and averaged over the azimuthal angle φ , this cross section is given by (Canuto, Lodenquai, Ruderman 1971; Herold 1979; Ventura 1979; Wasserman and Salpeter 1980; Harding and Daugherty 1991; Graziani 1993; first term on right-hand-side of eq. [2]):

$$\frac{d\sigma^r}{d\Omega_s^r} = \frac{d\sigma_{0 \rightarrow 0}^r}{d\Omega_s^r} + \frac{d\sigma_{0 \rightarrow 1 \rightarrow 0}^r}{d\Omega_s^r}, \quad (8)$$

where

$$\frac{d\sigma_{0 \rightarrow 0}^r}{d\Omega_s^r} \equiv \frac{3}{16\pi} \sigma_T \left[\sin^2 \theta^r \sin^2 \theta_s^r + \left(\frac{E^r}{E^r + E_B} \right)^2 \left(\frac{1 + \mu^{r2}}{2} \right) (1 + \mu_s^{r2}) \right] \quad (9)$$

is the continuum part of the cross section and

$$\frac{d\sigma_{0 \rightarrow 1 \rightarrow 0}^r}{d\Omega_s^r} \equiv \frac{9}{32} \frac{\sigma_T m_e c^2}{\alpha} \left[\frac{4E^{r3}}{E_B(E^r + E_B)^2} \right] \frac{\Gamma_1/2\pi}{(E^r - E_1^r)^2 + (\Gamma_1/2)^2} \frac{1 + \mu^{r2}}{2} \frac{1 + \mu_s^{r2}}{2} \quad (10)$$

is the resonant part. We use the exact relativistic resonant energy for the n^{th} harmonic $E_n^r = 2nbm_e c^2 / [1 + \sqrt{1 + 2nb(1 - \mu^{r2})}]$ with $n = 1$ in the Lorentzian factor in eq. (10). The subscript s denotes parameters of the scattered photon.

For a $0 \rightarrow 0$ scattering we obtain the total continuum scattering cross section σ_0^r by integrating eq. (9) over the scattered angle. We define σ_n^r as the total cross section for the resonant absorption that initiates a (resonant) scattering at the n^{th} harmonic. For $n \geq 1$, this is given by (Daugherty and Ventura 1977; Fenimore *et al.* 1988):

$$\sigma_n^r = \frac{3}{8} \frac{\pi m_e c^2 \sigma_T}{\alpha} b^{n-1} \frac{(n^2/2)^{n-1}}{(n-1)!} (1 + \mu^{r2})(1 - \mu^{r2})^{n-1} \frac{\Gamma_n/2\pi}{(E^r - E_n^r)^2 + (\Gamma_n/2)^2}. \quad (11)$$

In order to achieve greater accuracy in the first harmonic line wings, we use the value of σ_1^r obtained by integrating eq. (10) over the scattered angle rather than using eq. (11) which is strictly valid only near line center. The two expressions converge when $E^r \rightarrow E_1^r$. For the higher harmonics, we use eq. (11).

From the Lorentz invariance of $\tau/|\mu_{sl}|$ (see, e.g., Rybicki and Lightman 1979), the lab frame cross section σ_n is related to σ_n^r by

$$\sigma_n = (1 - \beta\mu) \sigma_n^r . \quad (12)$$

We average this cross section over $f(p)$, the one-dimensional electron momentum distribution, and divide by σ_T in order to obtain the dimensionless scattering profile for the n^{th} harmonic,

$$\phi_n(E, \Omega) \equiv \frac{1}{\sigma_T} \int dp f(p) \sigma_n . \quad (13)$$

The total scattering profile is approximately the sum of the profiles for the individual Landau levels (including the continuum contribution):

$$\phi(E, \Omega) \equiv \frac{1}{\sigma_T} \int dp f(p) \int d\Omega_s \frac{d\sigma}{d\Omega_s} \approx \sum_{n=0}^{\infty} \phi_n(E, \Omega) \quad (14)$$

(Wasserman and Salpeter 1980; Wang, Wasserman, and Lamb 1993).

Figures 2a, b, and c show the scattering profiles $\phi_0(E, \Omega)$, $\phi_1(E, \Omega)$, and $\phi_0(E, \Omega) + \phi_1(E, \Omega)$ vs. E for $B_{12} = 3.5$, $T_e = 10$ keV, and $\mu = 0, 0.5$, and 1 , respectively. It is clear from the figure that the line can be divided into the line core ($|x_n/\mu| \ll 1$) and the line wings ($|x_n/\mu| \gg 1$), where $x_n \equiv (E - E_n)/E_d^n$ is the dimensionless frequency shift (Wasserman and Salpeter 1980). In the line core, the thermal electron distribution dominates the profile so that $\phi_n \propto \exp[-(x_n)^2/|\mu|]$. In the wings, the tail of the Lorentzian distribution dominates so that $\phi_n \propto a(x_n)^{-2}$. We refer to the wing at energies below the line center as the red wing and the wing at energies above the line center as the blue wing. Wasserman and Salpeter (1980) showed that for the first harmonic, the core-wing boundary appears at $|x_1/\mu| \approx 2.62 - 0.19 \ln(100 a/\mu)$. Similarly, we define the wing-continuum boundary as the frequency shift where the profile for wing scattering along

the slab normal is equal to the profile for continuum scattering. From eqs. (9) and (10), we see that for $\Psi = 0$ this boundary occurs for the first harmonic at $|x_1| = 0.732 E_B/E_d^1$ in the red wing and $|x_1| = 2.73 E_B/E_d^1$ in the blue (cf. Figure 2c).

The dependence of the resonant cross section on photon energy is not strictly Lorentzian. There is a non-Lorentzian factor, $4E^{r3}E_B^{-1}(E^r + E_B)^{-2}$, shown in square brackets in eq. (10). In Figure 2d, e, and f, we compare $\phi_0 + \phi_1$, calculated with and without the non-Lorentzian factor, for $\mu=0.0, 0.5$, and 1.0 respectively. The profile is unaffected at the line center where the non-Lorentzian factor is equal to unity. However, this factor changes the profiles considerably in the wings. It raises the value of ϕ_1 in the blue wing, but ensures that $\phi_1 \rightarrow 0$ as $E \rightarrow 0$. This has a significant effect on the total profile as $\mu \rightarrow 1$, where ϕ_0 also goes to zero at low energies. It is clear from the figure that the non-Lorentzian factor can be ignored when the line wings are optically thin. Consequently, Wang *et al.* (1989) did not include it in their simulations. But, as we shall show, the non-Lorentzian factor significantly alters the properties of radiation emerging from line-forming regions that are optically thick in the wings. We therefore include it in our calculations for large optical depths.

The code used by Wang *et al.* required the magnetic field to be oriented along the slab normal ($\Psi = 0$). When this is the case, the line-forming region is azimuthally symmetric. Consequently, the original code only needed to keep track of the polar angle θ of a photon's orientation; it ignored the azimuthal angle φ . When $\Psi \neq 0$, the symmetry is broken, as shown in Figure 1a. Thus, in the present work, we modify the code to keep track of both angles (θ_{sl} and φ_{sl}) and bin the output accordingly. However, we continue to use cross sections that are averaged over the azimuthal angle, φ . The φ -dependent part of the scattering cross section is only significant in the line wings and continuum; in the present work we consider line-forming regions that are either not optically thick in the wings or are

azimuthally symmetric.

Lamb *et al.* (1989) showed that relativistic kinematics has a significant effect on the shape of the absorption profile, even in the limit $E, kT_e \ll m_e c^2$. We therefore use relativistic kinematics throughout this calculation, except where we indicate otherwise. For zero natural line width, relativistic kinematics prohibits scattering at the n^{th} harmonic above a cutoff frequency $E_c = (\sqrt{1 + 2nb} - 1) m_e c^2 / \sqrt{1 - \mu^2}$ (Daugherty and Ventura 1978; Harding and Daugherty 1991; see Appendix of Wang, Wasserman, and Lamb 1993 for a physical derivation). Wasserman and Salpeter (1980) show that under physical conditions where electron recoil is important, photons escape more readily in the red wing than in the blue. Since there was less of a focus on the blue wing, and for simplicity, Lamb *et al.* (1989), Wang *et al.* (1989), and Wang, Wasserman, and Lamb (1993) took the resonant scattering profile to be zero for $E > E_c$, ignoring the effects of the finite natural line width. For $E < E_c$, the effects of finite line width *were* included. The absence of resonant scattering above $E_c(\mu)$ gave rise to a spike at small μ just blueward of the first harmonic in some of the spectra generated by the original Monte Carlo code. This spike contained photons which were scattered to energies above E_c , either by scattering at the first harmonic or by photon spawning due to Raman scattering at the second or third harmonics, and which then escaped the atmosphere without further scattering (the probability of *continuum* scattering is finite but very small in the thin slabs used). In the present work, we include the effect of finite natural line width for $E > E_c$ so that the resonant scattering profile is now small but finite above E_c . With this enhancement, the spikes are smeared by scattering and no longer appear. However, we stress that, even though the scattering profile is finite above the cutoff energy when the effects of natural line width are properly treated, the profile still falls off sharply above E_c , leading to a strongly asymmetric line shape at small μ .

We do not include nonresonant inverse magnetic bremsstrahlung in our calculation.

This is justified since we are interested in high photon energies ($\gg 1$ keV) and small column depths. Specifically, photons with energy E originating from a depth $N_{e,21} > N_{e,21}^{th}$, where

$$N_{e,21}^{th} \approx 5.8 \times 10^4 \left(\frac{kT_e}{5 \text{ keV}} \right)^{1/3} \left(\frac{E}{20 \text{ keV}} \right)^{7/6} \quad (15)$$

(see, e.g., Nelson, Salpeter, and Wasserman 1993), will be thermalized before escape. For all cases we study in the present work, the column depth $N_{e,21} < N_{e,21}^{th}$.

4. Scattering Energetics and the Equilibrium Compton Temperature

When a photon scatters off an electron, energy is exchanged, either heating or cooling the atmosphere. The Compton equilibrium temperature T_c is defined as the temperature where the heating and cooling, summed over all scatters, balance exactly. For media optically thin in the continuum, the temperature is determined by resonant scattering. The resonant Compton temperature is reached on time scales which are short compared to most time scales of interest, such as the burst and dynamical time scales (see Lamb, Wang, and Wasserman 1990, hereafter LWW). We therefore calculate spectra for atmospheres at the resonant Compton temperature, except where we indicate otherwise. Consequently, it is important to understand how this temperature is affected by the geometry of the line-forming region.

To gain physical insight into the dependence of the resonant Compton temperature on the field angle Ψ , we first calculate T_c analytically in the single scattering limit (valid for line-forming regions which are optically thin in the first harmonic). We present this calculation in Section 4.1. In Section 4.2, we present results for T_c obtained from Monte Carlo simulations for line-forming regions that are optically thick in the line core, but not

in the wings. We discuss line-forming regions that are also optically thick in the wings and the continuum in Section 4.3.

4.1. Small Optical Depths

The single scattering analytic calculation of T_c applies in the limit of column depths small enough that the medium is optically thin at the first harmonic. Our treatment is similar but not identical to the analytic treatment of LWW. In their treatment, LWW used the resonant single scattering power to calculate T_c . Thus, their treatment depended solely on the distribution of injected photons with respect to the magnetic field (i.e., on the direction of the non-yrating component of the electrons' velocities); it did not address the particular geometry of the scattering medium. In the present analytic treatment, we explicitly consider an optically thin slab geometry and study the dependence of T_c on Ψ . In the evaluation of T_c , we assume an isothermal atmosphere which is threaded by a magnetic field whose strength is much less than the critical field B_{crit} and where the electron temperature T_e is much less than m_e (we use $\hbar = c = k = 1$ throughout Section 4).

To calculate the Compton temperature, we require that the *net* power in scattered photons, that is, the scattered power minus the incident power, be equal to zero. Equivalently, the heating and cooling of the atmosphere by the plasma exactly balance at $T_e = T_c$ so that the total energy change of the photons ΔE , which has been summed over scatters and averaged over the scattering photon distribution, is equal to zero. Working in the lab frame, we have

$$\Delta E \equiv \frac{\int d\Omega dE n(E, \Omega) \overline{\delta E} N_{\text{scat}}(\tau_{T_o}, E, \Omega)}{\int d\Omega dE n(E, \Omega)}, \quad (16)$$

where $n(E, \Omega) dE d\Omega$ is the scattering photon number density in the interval (E, Ω) to

$(E + dE, \Omega + d\Omega)$ (assumed constant throughout the medium), $N_{scat}(\tau_{To}, E, \Omega)$ is the total number of scatters experienced by a photon injected from position τ_{To} inside the medium with energy E and direction of propagation Ω , and $\overline{\delta E}$ is the mean energy change per electron-photon scattering.

Setting $\Delta E = 0$ thus gives the slab Compton temperature

$$\frac{T_c}{E_B} = \frac{1}{10} \frac{\int \frac{d\Omega}{|\mu_{sl}|} Q(\Omega) (2 + 7\mu^2 + 5\mu^4)}{\int \frac{d\Omega}{|\mu_{sl}|} Q(\Omega) [1 + (s + 2)\mu^2 + (s - 3)\mu^4]} . \quad (\text{A14})$$

The derivation is given in the Appendix. In arriving at this expression we have assumed a separable scattering photon number density

$$n(E, \Omega) = n(E) Q(\Omega) \quad (\text{A8})$$

with

$$s \equiv - \frac{E}{n(E)} \left. \frac{dn}{dE} \right|_{E=E_B} , \quad (\text{A12})$$

and used a non-relativistic one-dimensional Maxwellian for the electron momentum distribution along the field.

The most natural coordinate system to use to evaluate T_c is the slab coordinate system (cf. Figure 1), that is, $d\Omega = d\mu_{sl} d\varphi_{sl}$, where

$$\mu = \mu_{sl} \cos \Psi + \sqrt{1 - \mu_{sl}^2} \sin \Psi \cos \varphi_{sl} . \quad (\text{17})$$

For injection along the slab normal, $Q(\Omega) \propto \delta(\mu_{sl} - 1)$, $\mu = \cos \Psi$, and eq. (A14) gives

$$\frac{T_c}{E_B} = \frac{1}{10} \frac{2 + 7 \cos^2 \Psi + 5 \cos^4 \Psi}{1 + (s + 2) \cos^2 \Psi + (s - 3) \cos^4 \Psi} . \quad (18)$$

This reduces to the values found by LWW for injection along the field,

$$\Psi = 0, \quad \frac{T_c}{E_B} = \frac{T_c^{\parallel}}{E_B} \equiv \frac{7}{10s} , \quad (19)$$

and injection orthogonal to the field,

$$\Psi = \pi/2, \quad \frac{T_c}{E_B} = \frac{T_c^{\perp}}{E_B} \equiv \frac{1}{5} , \quad (20)$$

as it must. If the initial photon distribution covers a range of angles, we expect the Compton temperature to fall between the two extremes given in eqs. (19) and (20).

The $1/|\mu_{sl}|$ factor in eq. (A14) originates from the slab geometry [i.e., eq. (A3)]. It indicates that the dominant contribution comes from photons traveling at large angles to the slab normal, since these photons have the largest probability of scattering. However eq. (A14) is valid only when $\tau/|\mu_{sl}| \ll 1$ [cf. eqs. (A2), (A3), and (A5)], so the case of isotropic injection must be treated with some care. For first harmonic scattering,

$$\tau(E = E_B, \Omega) \approx \frac{\tau_1}{\sqrt{\pi}} \frac{3(1 + \mu^2)}{4|\mu|} , \quad (21)$$

where τ_1 is given by eq. (4). For a given $\tau_1 < 1$, there is some critical $|\mu_{sl}^c|$ above which eq. (A14) is valid. Thus, for example, when $\Psi = 0$ and $\tau_1 \ll 1$, $\tau/|\mu_{sl}| < 1$ when $|\mu_{sl}| > |\mu_{sl}^c| \approx (3\tau_1/4\sqrt{\pi})^{1/2}$. When $|\mu_{sl}| < |\mu_{sl}^c|$, the single scattering approximation fails. When eq. (17) is substituted into eq. (A14) and photon injection is isotropic or semi-isotropic (i.e. isotropic over a hemisphere), the integrands in equation (A14) have terms of order μ_{sl}^{-1} , μ_{sl} , and μ_{sl}^3 . If τ_1 (and therefore $|\mu_{sl}^c|$) is small enough, eq. (A14) will

be valid at sufficiently small values of μ_{sl} so that the μ_{sl}^{-1} terms dominate the integrals. We thus have, for semi-isotropic injection,

$$\frac{T_c}{E_B} = \frac{1}{10} \frac{16 + 28 \sin^2 \Psi + 15 \sin^4 \Psi}{8 + 4(s + 2) \sin^2 \Psi + 3(s - 3) \sin^4 \Psi} . \quad (22)$$

For $\Psi \rightarrow 0$, $T_c/E_B \rightarrow T_c^\perp/E_B \equiv 1/5$, because the dominant contribution comes from photons traveling nearly orthogonal to the slab normal and hence the field. As Ψ increases, so does T_c , due to the contribution of photons traveling at smaller angles to the field. For $\Psi \rightarrow \pi/2$, $T_c/E_B \rightarrow 59/70(1 + s)$ which is different from the result for injection along the field ($T_c^\parallel/E_B = 7/10s$). This is because, although photons with small $|\mu_{sl}|$ are dominant, the isotropy in φ_{sl} means that photons travel at all angles relative to the field.

We have calculated T_c/E_B as a function of Ψ from eq. (22) for $s = 1$. The results are shown in Figure 3. The temperature rises from $T_c/E_B = T_c^\perp/E_B = 1/5$ when the field is along the slab normal ($\Psi = 0$) to $T_c/E_B = 59/140$ when the field is along the slab ($\Psi = \pi/2$). Figure 3 also shows Monte Carlo calculations for $B_{12}=1.70$ and $N_{e,21} = 6 \times 10^{-4}$ ($|\mu_{sl}^c| \approx 0.016$). We show the Monte Carlo calculations for both the approximate (non-relativistic) kinematics given by eq. (A7) and for exact relativistic kinematics. The analytic model and the *non-relativistic* Monte Carlo calculation show good agreement, as they should. The value of T_c differs between the relativistic Monte Carlo calculation and the analytic one by amounts up to \sim a few times $E^r/2m_e$. We attribute the differences between the two calculations to the higher order terms in $E^r/2m_e$ which were not included in the kinematics in the analytic model (eq. (A7)). Using exact relativistic kinematics, there are two roots for the electron momentum, p_{min} and p_{max} (see, e.g., Daugherty and Ventura 1978; Harding and Daugherty 1991; Wang, Wasserman, and Lamb 1993). This is in contrast to the single root for the non-relativistic kinematics used in our analytic model. Scattering via the p_{max} channel involves fast moving, i.e., higher

β , electrons, and is rare for the electron temperatures we consider; typically 1-2% of all scatters access the p_{max} channel in the relativistic Monte Carlo simulations shown in Figure 3. However, more energy is transferred to the photons in these rare events with the net result being that runs using relativistic kinematics including the p_{max} channel typically had more efficient electron cooling and hence lower T_c/E_B (for given Ψ) than runs without this channel. This is evident in Figure 3.

4.2. Moderate Optical Depths

At larger column depths, $\tau/|\mu_{sl}| > 1$ and eq. (A3) is no longer valid. Consequently, we need to consider the effects of multiple scatterings and we can not use our analytic treatment to calculate T_c . Instead we use our Monte Carlo code to calculate the emerging photon spectrum and determine the amount of energy transferred to the photons while passing through the slab. By varying the electron temperature we can determine the temperature at which the net energy transferred is zero. Using this technique, LWW calculate the Compton temperature for semi-isotropic injection in a line-forming region with a 1-0 geometry and $\Psi = 0$, column depths in the range $0.12 \leq N_{e,21} \leq 12$, and magnetic fields in the range $1.50 \leq B_{12} \leq 2.10$. They find that $T_c/E_B \approx 0.27$. In the ranges considered, they find the Compton temperature to be relatively insensitive to the magnetic field and to decrease slightly with increasing column depth.

In the present work, we fix the column depth and magnetic field and study the effects of the source plane position and the field orientation, as well as the effects of the higher harmonics and the natural line width. We use $N_{e,21}=1.2$, $B_{12}=1.70$, and a power law injected spectrum with $s = 1$. Figure 4 shows the Compton temperature T_c/E_B as a function of the field orientation for both the 1-0 and 1-1 geometries. The temperatures are

generally higher than in the optically thin case. The increase is most dramatic when the field is parallel to the slab normal ($\Psi = 0$). To understand this, recall that in the optically thin case, almost all photons that scatter are moving perpendicular to the slab normal, and therefore have $\mu = \mu_{sl} \approx 0$ when $\Psi = 0$. However, in the optically thick case, there is an increase in the number of photons moving at larger values of μ before scattering, which raises the Compton temperature (cf. eqs. [19], [20]). The increase in high μ photons that scatter is due to the increased optical depth for photons moving parallel to the field (along the slab normal), and the multiple scattering of photons that were injected perpendicular to the field (along the slab).

While the analytic model assumes zero natural line width and includes first harmonic scattering only, the calculations shown in Figure 4 assume finite natural line width and include scattering at the first three harmonics. As shown in table 1, the effect of the finite line width and higher harmonics is small.

As we increase the column depth to $N_{e,21} = 12$, we find a small *increase* in Compton temperature, in contrast to the results of LWW. The difference is due to the effects of blue wing scattering. Because higher energy photons are able to scatter, the cooling of the electrons is less efficient, which raises the Compton temperature.

4.3. Large Optical Depths

In a closed system in thermal equilibrium, in which the photon density is low enough that stimulated scattering can be ignored, the photons have a Wien distribution with temperature $T_\gamma = T_e$ (see, e.g. Rybicki and Lightman 1979). There is no net energy transfer between the photons and the electrons, and the photons have an isotropic angular distribution, i.e. $N(E) = 0$, where $N(E)$ is the net photon flux. We expect that at optical

depths that are large enough so that $\tau \gg 1$ and the flux to density ratio, $N(E)/(cn(E)) \ll 1$, the photons behave approximately as in a closed system.

In section 4.2 we discussed scattering energetics in line-forming regions that are optically thick in the line core and optically thin in the wings and the continuum. In this section we examine the effects of larger optical depths by considering line-forming regions with $\Psi = 0$, $B_{12} = 3.5$, and $N_{e,21} = 15,000$ ($\tau_{To} = 10$). The line-forming region is optically thick in both the line wings ($a\tau_1 \gg 1$) and the continuum ($\tau_{To} \gg 1$). For comparison, we also consider a line forming region with $N_{e,21} = 1,500$ ($\tau_{To} = 1$), which is optically thick in the wings but only marginally thick in the continuum, and a line-forming region with $N_{e,21} = 30$ ($\tau_{To} = 0.02$) which is marginally optically thick in the wings and optically thin in the continuum. All three line-forming regions are optically thick in the line core ($\tau_1 \gg 1$). The key parameters for the runs are listed in Table 2. In addition, the mean number of scatters experienced per escaping photon, N_{scat} , and the mean energy of escaping photons (averaged over the emerging photon distribution; see below) are listed.

To simulate the behavior of a system with large optical depth, we inject a Wien spectrum with $T_\gamma = T_e$. For T_e , we adopt a fiducial value of $kT_e/E_B = 1/4$, which is approximately the Compton temperature for resonant scattering (cf. Section 4.2). We include only continuum and first harmonic scattering in these calculations. Higher harmonics are not important, due to the exponential rollover in the continuum spectrum which occurs well below the first harmonic. Thus, eq. (2) with only the first term on the right hand side is a valid approximation for these simulations, even for line-forming regions that are optically thick in the line wings.

As Table 2 shows, at the largest optical depths, the mean energy of the transmitted photons is considerably smaller than the mean injected energy. For example, for $N_{e,21} = 15,000$ ($\tau_{To} = 10$) and the 1-1 geometry, the mean energy of the transmitted

photons is 15.5 keV, compared to a mean energy of $3kT_\gamma = 30$ keV for the injected photons. Most of the energy redistribution occurs deep in the slab, as shown in Figure 5. Here we plot $\langle E_t(\tau_T) \rangle$, the mean photon energy associated with the net (upward) flux crossing a given plane inside the slab and is calculated from

$$\langle E_t(\tau_T) \rangle = \frac{\int_0^\infty dE E [N_{\text{up}}(E, \tau_T) - N_{\text{down}}(E, \tau_T)]}{\int_0^\infty dE [N_{\text{up}}(E, \tau_T) - N_{\text{down}}(E, \tau_T)]}. \quad (23)$$

At the edge of the atmosphere, $N_{\text{down}}(E, \tau_T = 0) \equiv 0$, and $\langle E_t(\tau_T = 0) \rangle$ becomes simply the mean energy of escaping photons averaged over the emergent photon distribution (cf. last column in Table 2).

It is evident from this figure that an optical depth of $\tau_T = 10$ is not sufficient for thermal equilibrium between the electrons and the photons. On the contrary, as the photons move upwards they steadily lose energy to the electrons until they reach a depth of about $\tau_T = 7$. Above this depth, the shape of the spectrum is altered by multiple scattering, but the mean energy of the distribution remains the same until the photons get close to the surface. Above $\tau_T \approx 0.004$, the line wings are optically thin and there is a slight increase in $\langle E_t(\tau_T) \rangle$.

The reason that thermal equilibrium does not occur at $\tau_T = 10$ is apparent in eq. (9) and Figure 2c. For $E \ll E_B$, the scattering profile for a $\mu = 1$ photon decreases with energy like $(E/E_B)^2$. Thus, at *any* depth τ_T , there exists some energy, $E_{\text{thin}}(\tau_T)$, such that the plasma appears optically thin to $\mu = 1$ photons with $E < E_{\text{thin}}(\tau_T)$. If τ_T is large enough so that $E_{\text{thin}} \ll E_B$, then from eqs. (8)-(10),

$$\frac{E_{\text{thin}}(\tau_T)}{E_B} = \left(\frac{2 + \tau_T + \sqrt{8\tau_T + \tau_T^2}}{2} \right)^{-1/2}. \quad (24)$$

Because of the strong angle and frequency dependence of the cross section in a strong magnetic field, the use of the Thomson depth to indicate optical depth in the continuum is misleading. Even at $\tau_T = 10$, a significant number of photons can escape without scattering.

The energy shift in Figure 5 occurs because photons diffuse in angle- and frequency-space until their angle with the magnetic field is small and $E \lesssim E_{\text{thin}}(\tau_T)$. They are then able to escape without further scattering. The importance of this redistribution is illustrated by comparing the cumulative spectrum of the emerging photons with that of the injected photons, as shown in Figure 6. As the figure shows, even though only 14% of the photons are injected with $E < E_{\text{thin}}(7) = 12.9$ keV, 45% escape below this energy. This effect could be even more pronounced if we did not use polarization-averaged cross sections; at low energies, the scattering profile for extraordinary mode photons goes like $(E/E_B)^2$, regardless of the direction they are traveling.

To test the hypothesis that the shift in the photon energies is due to the form of the scattering cross section at low E , we ran a 1-1, $N_{e,21} = 15,000$ ($\tau_{T_0} = 10$) simulation in which the non-Lorentzian factor was removed from the scattering cross section. As Figure 2f shows, without this factor, the scattering profile approaches σ_T as $E \rightarrow 0$, so the line-forming region is no longer optically thin to low energy photons. As shown in Table 2, $\langle E_t(0) \rangle = 24.7$ keV in this simulation, much larger than in the simulation with the non-Lorentzian factor included. In addition, without the non-Lorentzian factor, the ratio $N(E)/(cn(E))$ remains much smaller than unity through most of the slab, as expected for a thermal distribution of photons. Clearly the detailed behavior of the scattering cross section plays an important role in forming the redshifted spectrum of the escaping photons.

The transfer of energy from the photons to the electrons deep in the slab implies that the electron temperature $T_e = E_B/4$ assumed in the calculation is less than the Compton temperature at large depths. In this situation, the photons will heat the electrons until

T_C is reached. However, as Figure (5) indicates, T_e already equals T_C above $\tau_T \approx 7$. The shape of the curve indicates that a self-consistent calculation requires a temperature profile, $T_e(\tau_T)$, rather than a constant value of T_e throughout the slab. This result is consistent with the finding of Bulik (1993) that T_e rises slightly below $\tau_T \sim$ a few (see also Nagel 1981; Miller, Wasserman, and Salpeter 1989). The temperature profile could be implemented by dividing the slab into several zones with different electron temperatures, as suggested by LWW.

5. Monte Carlo Spectra

Our Monte Carlo simulations reveal a rich variety of line properties which vary with the viewing angle, the magnetic field orientation, the optical depth, and the slab geometry. For line-forming regions that are optically thick in the line core, but optically thin in the line wings and the continuum, we discuss the line shapes in Section 5.1 and the equivalent widths in Section 5.2. These simulations reveal prominent shoulders on both sides of the first harmonic line when the radiation is viewed at $\mu_{sl} \gtrsim 0.25$, regardless of the field orientation. We discuss the line shoulders in Section 5.3. In Section 5.4 we consider line-forming regions that are optically thick in the line wings and the continuum, in addition to the core.

5.1. Line Shapes for Moderate Optical Depths

Figures 7, 8 and 9 show Monte Carlo scattering spectra for $\Psi = 0$, $\Psi = \pi/4$, and $\Psi = \pi/2$, respectively. In all three figures, the column depth is $N_{e,21} = 1.2$, which is optically thick in the line core and optically thin in the wings. We include results for both the 1-0 and 1-1 geometries and for several viewing angles. To produce the $\Psi = 0$ spectra,

we inject a total of one million photons into the slab isotropically and record the photons emerging from the slab in one of eight bins in μ_{sl} ($0 < \mu_{sl} \leq 1$). To produce the $\Psi \neq 0$ spectra, we inject eight million photons and record the emerging photons in 80 angular bins (10 bins in φ_{sl} between 0 and π for each of 8 bins in μ_{sl}). In each panel the 1-1 spectrum is normalized to have unit area and the 1-0 and pure absorption spectra are normalized to match the 1-1 spectrum in the continuum.

For comparison, we also show pure absorption spectra,

$$N_{abs}(E, \Omega_{sl}) = N_i(E) \exp\left(-\frac{N_e \sigma_T \phi}{|\mu_{sl}|}\right), \quad (25)$$

where the scattering profile ϕ is given by eq. (14). $N_{abs}(E, \Omega_{sl})$ is the spectrum in which photons that have undergone the absorption that initiates a resonant scatter are not re-emitted. We can explain many of the properties of the spectra in terms of the scattering profile and the geometry of the line-forming region.

The second and third harmonics have shapes similar to absorption lines because most of the photons that scatter at these energies are Raman scattered — i.e., they are absorbed and then re-emitted as two or three lower harmonic photons. The line properties of the higher harmonic features can therefore be understood in terms of eq. (25) and the scattering profiles. To illustrate this, we combine eqs. (11), (12), (13), and (A13) and let $\Gamma_n \rightarrow 0$ and $\beta \ll 1$ to get the non-relativistic resonant scattering profile for the n^{th} harmonic with zero natural line width,

$$\phi_n \approx \frac{3\pi}{8\alpha} b^{n-1} \frac{(n^2/2)^{n-1}}{(n-1)!} (1 + \mu^{r2})(1 - \mu^{r2})^{n-1} \frac{\exp\left[-\left(\frac{E-E_n}{E_d^n \mu}\right)^2\right]}{\sqrt{\pi} E_d^n |\mu|}. \quad (26)$$

It is evident from eqs. (26) and (25) that while the Doppler factor $E_d^n |\mu|$ broadens the lines

when viewed *along the field*, the line-of-sight column depth $N_e/|\mu_{sl}|$ deepens the lines when viewed *along the slab*. Thus, when the magnetic field is parallel to the slab normal ($\Psi = 0$), the lines become deeper and narrower as the viewing angle moves from $\mu_{sl} = 1$ to $\mu_{sl} = 0$ (Figure 7). When the field is perpendicular to the slab normal however ($\Psi = \pi/2$), these two effects combine to provide especially broad and deep lines when viewed perpendicular to the slab normal and at modest angles to the magnetic field (e.g., Figure 9k). When the viewing angle is directly *along* the field (e.g., Figures 7a and 9j), the scattering profile for the higher harmonics is dominated by the $(1 - \mu^{r2})^{n-1}$ factor and the higher harmonics are suppressed.

The properties of the first harmonic are determined by multiple scatterings and photon spawning. Consequently, there is no simple analytic expression that describes the first harmonic scattering line. However, though the physics of line-formation are fundamentally different, the full-width half-maximum of the first harmonic *scattering* line tends to be similar to that of the first harmonic *absorption* line. Thus, eqs. (25) and (26) do provide some insight into the first harmonic. Up to a logarithmic factor $\sim (\ln \tau_1)^{1/2} \sim 1$, the Doppler width dominates the width of the first harmonic line. This is because $\delta E/E \ll 1$ in core scattering and there is negligible frequency redistribution in the line wings for the cases we study in Figures (7)–(9).

5.2. Line Equivalent Widths for Moderate Optical Depths

The equivalent width of the first harmonic line is plotted as a function of viewing angle in Figures 10, 11, and 12. In calculating the first harmonic equivalent width, we need to adjust for any overlap between the first and second harmonic lines in the emergent spectra. For column depths $N_{e,21}/|\mu_{sl}| \gtrsim 6(kT_e/1 \text{ keV})$, the line wings of the first harmonic can

have optical depths $\gtrsim 1$ so frequency redistribution in the line wings can be significant. Thus, at large values of $N_{e,21}$ or small values of $|\mu_{sl}|$, the first and second harmonics begin to overlap (see, e.g., Figure 9j). To correct for this, we assume that the second harmonic is approximately an absorption line and we calculate the equivalent width of the first harmonic according to:

$$W_{E1}(\Omega_{sl}) = \int \frac{N_i(E)g_2(E, \Omega_{sl}) - N(E, \Omega_{sl})}{N_i(E)g_2(E, \Omega_{sl})} dE \quad (27)$$

where $N(E, \Omega_{sl})$ is the transmitted spectrum and $g_2(E, \Omega_{sl})$ is as defined in eq. (25) with $\phi \rightarrow \phi_2$. We stress that this formula *assumes* the spectrum $N(E, \Omega_{sl})$ is accurate and merely corrects for the overlap in the calculation of W_{E1} . It *does not* correct for the inaccuracy in our modeling of the transfer through a scattering medium that could be optically thick in the line wings (cf. eq. 2 and associated discussion).

We display W_{E1} for slabs with $\Psi = \pi/2$ in Figure 10 for the 1-0 geometry and in Figure 11 for the 1-1 geometry. $B_{12} = 1.7$ and $N_{e,21} = 1.2$ in both figures. For viewing along the slab (small μ_{sl}), the equivalent width decreases as the azimuth φ_{sl} moves from 0 to $\pi/2$. This is because the scattering profile for the first harmonic, unlike the higher harmonics, has no $1 - \mu^2$ factor that causes the cross section to vanish along the field. Photons propagating along the field see a larger cross section and Doppler width which tends to scatter them out of the line of sight, while photons propagating orthogonal to the field see a reduced scattering cross section and Doppler width which reduces the chance of scattering. As μ_{sl} increases, the equivalent width decreases because photons escape more easily in directions transverse to the slab where the column depth is lower.

We display W_{E1} for slabs with $\Psi = 0$ and compare the results with those for $\Psi = \pi/2$ in Figure 12. The figure also illustrates the dependence of equivalent width (W_{E1}) on

column depth. The figure shows W_{E1} as a function of μ_{sl} for $B_{12}=1.7$ for $N_{e,21}=0.12, 1.2,$ and 12; and for both the 1-0 and 1-1 geometries. The azimuthal angle is $0 < \varphi_{sl} < \pi/8$ for $\Psi = \pi/2$ and $0 < \varphi_{sl} < 2\pi$ for $\Psi = 0$. The figure shows that the geometry can have a larger effect on the equivalent width than the column depth does. For all geometries, the equivalent widths are largest when the spectrum is viewed along the slab ($\mu_{sl} \rightarrow 0$). In the 1-0 geometry with $\Psi = 0$, increasing the column depth two orders of magnitude from $N_{e,21}=0.12$ to 12 increases the width at $0 < \mu_{sl} < 1/8$ from $W_{E1}/E_B = 0.096$ to 0.39. However, keeping $N_{e,21}$ at 0.12 but rotating the field so it lies along the slab increases the equivalent width in this μ_{sl} bin from $W_{E1}/E_B = 0.096$ to 0.64.

As μ_{sl} approaches unity, the equivalent width decreases and can become negative. This is especially true for the 1-1 geometry. A negative equivalent width corresponds to an emission-like feature. The presence of such a feature in an angular bin requires a surplus of photons emerging in the bin compared with the number of photons that were injected. In Figures 7-9, such features appear as shoulders on either side of the line center. The shoulders are very prominent in the 1-1 geometry, but less so in the 1-0. For example, as we see in Figure 12d, $W_{E1}/E_B=-0.96$ in the $7/8 < \mu_{sl} < 1$ bin in the 1-1 geometry, but only -0.066 in the 1-0. Physically, these shoulders are the result of angular and frequency redistribution in electron-photon resonant scattering.

5.3. Line Shoulders

Many authors discuss line shoulders. Wasserman and Salpeter (1980) predict that for physical conditions where electron recoil is important (e.g., accretion-powered pulsar line-forming regions), there is an excess of photons escaping in the red wing compared with the blue. Alexander and Mészáros (1989), Nishimura and Ebisuzaki (1992), and Nishimura

(1994) report shoulders in spectra generated by Feautrier calculations with 1-0 geometries and $N_{e,21}$ varying from ~ 0.1 to ~ 100 . The shoulders reported by Alexander and Mészáros (1989) are small, in agreement with our 1-0 results. In contrast, Nishimura (1994) finds very large shoulders with $W_{E1}/E_B < -10$ in some cases. Further, he reports that the shoulders are most prominent at *small* μ_{sl} , in direct contradiction to our results. Araya and Harding (1996) also report shoulders, which they observe in spectra generated by a Monte Carlo code for both 1-1 and cylindrical geometries with column depths up to $N_{e,21} \sim 5$. In this section, we develop a better understanding of line shoulders by investigating how they are affected by viewing angle, spawning, electron temperature, and source plane position.

Chandrasekhar (1960) shows that photons that scatter isotropically in a slab atmosphere emerge disproportionately at high μ_{sl} because of the lower column depth along the slab normal. The tendency of photons to emerge at high μ_{sl} is the reason the shoulders in the present calculation become more prominent as $\mu_{sl} \rightarrow 1$. The shoulders are weak or nonexistent for low μ_{sl} because the enhanced column depth along the slab ensures that most photons are scattered out of the line of sight, resulting in the formation of absorption-like features. Figure 13 displays Monte Carlo calculations of the emergent angular distribution of resonantly scattered photons. The photons are injected monochromatically at $E = E_B$ so that every photon scatters. As the figure shows, the number of photons *emerging* generally increases with μ_{sl} , even though they were *injected* isotropically. This is true for both the 1-0 and 1-1 geometries and for fields both parallel and perpendicular to the slab normal. In the 1-0 geometry (Figures 13a and c), there is an excess of reflected photons over transmitted photons because of the shorter path length for the former. This contrasts with the 1-1 geometry (Figures 13b and d), where the line forming region is symmetric about the source plane. There is no short escape path and the transmitted and reflected spectra are (by symmetry) identical. In both geometries, few photons escape along the slab owing to the large path length. In the $\Psi = 0$ case, escape along the slab normal is favored by both the

short path length and by a scattering cross section which is largest for a scattered photon direction $\mu_s = 1$. The emergent angular distribution peaks at $\mu_{sl} = 1$ (cf. Figures 13a,b). By contrast, in the $\Psi = \pi/2$ case, escape along the slab normal, while favored by the shorter path length, is discouraged by the scattering cross section. The emergent angular distribution is, therefore, peaked in a direction determined by a compromise between the most favored scattered angle ($\mu_{sl} \rightarrow 0$) and the shortest path length ($\mu_{sl} \rightarrow 1$) (cf. Figures 13c and d).

Figures 14 and 15 show spectra emerging from a line-forming region with a column depth $N_{e,21} = 1.2$ threaded by a field of strength $B_{12} = 1.7$ with $\Psi = 0$ and $\pi/2$, respectively. The injected photon spectrum is $\propto 1/E$. When the viewing angle is perpendicular to the slab normal, the scattered spectrum is similar to a pure absorption spectrum. When the viewing angle is parallel to the slab normal, shoulders can appear. It is evident from Figures 14a and b and 15a and b that spawning enhances the shoulders by providing an additional source of first harmonic photons. However, the shoulders are prominent in the 1-1 geometry even when spawning is not included in the calculation. This is because photons injected initially into the bottom half of the slab in the 1-1 geometry can escape through the top half after multiple scatters thereby providing an effective additional source of first harmonic photons (see Figure 17 below and associated discussion).

Figures 14 and 15 also reveal that the spacing of the line shoulders is of the same order as the width of the corresponding pure absorption lines. This simply reflects the fact that in media optically thin in the line wings the shoulder spacing is given approximately by the Doppler width $2E_d^1|\mu^{esc}|$ times a factor $\sim (\ln \tau_1)^{1/2} \sim 1$ as a result of multiple scatters (cf. Osterbrock 1962; Wang, Wasserman, Salpeter 1988).

The relative size of the red and blue shoulders is determined by the relationship between the electron temperature and the Compton temperature. At the Compton temperature, by

definition, the photons on average lose as much energy as they gain. We therefore expect the area under the two shoulders in the photon *energy* spectrum to be approximately equal when $T_e = T_c$.

As we see in Figures 16c and d, this is the case for a 1-1 slab atmosphere with $B_{12} = 1.7$, $N_{e,21} = 1.2$, $\Psi = 0$ and $\pi/2$, and a 1/E injected photon number spectrum. In order to illustrate the total change in energy of the photons, we use angle-integrated spectra in this figure. For $T_e < T_c$, the photons on average lose more energy than they gain and the red shoulder is larger (Figures 16a and b). This result is consistent with Alexander and Mészáros (1989), who use a temperature (5.2 keV) that is below the Compton temperature, and report a slightly greater flux in the red shoulder over the blue. For $T_e > T_c$, we find the blue shoulder is larger than the red, as expected (Figures 16e and f).

The line shoulders are more prominent in the 1-1 geometry than in the 1-0 at modest optical depths because of an excess in the flux of photons near the line center in the 1-1. We illustrate this for the case of $\Psi = 0$, $B_{12} = 1.7$, and $N_{e,21} = 1.2$. Figure 17 shows the angle-integrated flux of photons moving upwards ($\mu_{sl} > 0$) as a function of energy at four points in the slab: $\tau_T/\tau_{T_o}=1.00$ (the source plane), 0.32, 0.02, and 0.00 (the upper surface). At the source plane, the excess of photons in the 1-1 geometry takes the form of a prominent peak (Figure 17d). The reason for the peak is that as line photons scatter, they can cross the source plane many times. The peak contains photons which were injected towards the bottom of the slab ($\mu_{inj} < 0$), but which subsequently scattered upwards and crossed the source plane (an odd number of times, in general). The peak also contains photons which were injected towards the top of the slab ($\mu_{inj} > 0$), but which, in the course of multiple scatters cross the source plane twice (or, in general, an even number of times) — once downwards and once upwards. In other words, the photon flux in the 1-1 geometry, like the emergent spectrum, is the sum of transmitted and reflected components (cf. Section 2).

The two components contribute about equally to the peak. The peak does not appear in the 1-0 geometry because photons that are traveling downwards from the source plane have escaped the slab and are part of the reflected spectrum.

The peak is responsible for the prominence of the shoulders in the 1-1 geometry. As the photons in the peak move upwards through the slab their frequencies are redistributed in multiple scatterings — they are scattered out of the line — and shoulders form. Shoulders are diminished in the 1-0 geometry, compared to their appearance in the 1-1, because there is no photon excess near the line center. Note also the formation of the higher harmonic features, which, being effectively true absorption features, is essentially independent of geometry.

5.4. Large Optical Depths

In sections 5.1–5.3 we discussed the spectra emerging from line forming regions with a moderate column depth of $N_{e,21} = 1.2$ ($\tau_{T_o} = 0.0008$). But the emission regions of accretion-powered pulsars are thought to have column depths $N_{e,21} \sim 10^3 - 10^4$. In this section we discuss our Monte Carlo results for the emerging spectra for slabs with column depths in this range. Table 2, above, lists the key parameters for these simulations.

Figure 18 shows the angle-integrated flux of photons moving upwards ($\mu_{sl} > 0$) as a function of energy at four points in the slab: $\tau_T/\tau_{T_o}=1.00$ (the source plane), 0.32, 0.02, and 0.00 (the upper surface). As expected, the line becomes broader and deeper as the column depth increases. At $N_{e,21} = 15,000$, virtually no photons escape in the line core.

The $N_{e,21} = 30$ simulation shows a prominent red wing shoulder. The blue shoulder is less evident, due in part to the exponential decline of the injected spectrum above the line energy. At $N_{e,21} = 1,500$, substantial scattering in the wings significantly shifts the

centroids of the shoulders and broadens them. At $N_{e,21} = 15,000$, the slab is optically thick in the continuum. Scattering in the continuum broadens the shoulders so that they are no longer discernible.

The influence of the continuum can be seen in the mean number of scatters a photon experiences before escaping the slab. Taking a typical $\mu \sim 0.5$, we see from Figure 2 that continuum scattering dominates below ~ 20 keV. For $N_{e,21} = 30$ and 1,500, the mean energy of escaping photons is about 29 and 25 keV, respectively, so that photons escape primarily in the wings after multiple core-wing excursions (though for $N_{e,21} = 30$, the wings are only marginally thick). The number of scatters, N_{scat} , is then dominated by core and wing scatters. Since these scatters are accumulated mostly in the region where $T_e \sim T_C$ (cf. Figure 5), N_{scat} follows the zero recoil scaling, viz, $N_{scat} \propto \tau_1$ (Adams 1971; Wasserman & Salpeter 1980). For $N_{e,21} = 15,000$, the mean energy of escaping photons is about 15 keV, so that photons escape primarily in the continuum. In this case, photons enter the continuum after multiple core-wing excursions. Since the continuum is optically thick, they can return to the wings after many scatters in the continuum and escape in the continuum after a few such continuum-wing transitions. The addition of the continuum domain breaks the $N_{scat} \propto \tau_1$ scaling and increases N_{scat} above that expected for pure line transfer. This increase can be seen clearly in Table 2 where N_{scat} for runs both with and without the continuum are listed. For $\tau_{To} = 10$, core and wing scatters still dominate the total number of scatters so that $N_{scat} \propto \tau_1$ remains good to $\lesssim 20\%$. For much larger column depths, however, photons escape in the continuum only after many continuum-wing-core transitions, thereby resulting in much larger N_{scat} . Thus, at $\tau_{To} = 100$, for instance, we find $N_{scat} \approx 6 \times 10^6$ with the continuum turned on and about 1×10^6 with it turned off. The mean energy of escaping photons in this case is about 10 keV. The number of (line) scatters with continuum turned off ($\sim 10^6$) is less than that expected from the $N_{scat} \propto \tau_1$ scaling ($\sim 2 \times 10^6$) because this scaling ignores the non-Lorentzian factor (cf. eq. [10])

which substantially reduces the scattering cross section at very low energies.

5.5. Cylindrical Geometry

If the radiation from an accretion-powered pulsar emerges from the stellar surface, the spectrum is similar to the spectrum emerging from a 1-1 line-forming region with $\Psi = 0$. If the spectrum emerges from the sides of a cylindrical accretion column, however, it will be similar to that of a 1-1 line-forming region with $\Psi = \pi/2$ viewed in the $\varphi_{sl} \sim 0$ plane. We illustrate the latter case in Figure 19, which shows a Monte Carlo spectrum emerging from a cylindrical line-forming region. The magnetic field is oriented along the cylinder axis and has strength $B_{12} = 1.7$. The column depth, measured radially from the cylinder axis to the surface is $N_{e,21}=1.2$. A power law spectrum with $s = 1$ is injected along the cylinder axis. The figure shows that the cylindrical spectrum is qualitatively similar to a 1-1 spectrum with $\Psi = \pi/2$ viewed in the $\varphi_{sl} \sim 0$ plane. Shoulders appear in the spectrum at small values of μ (Figure 19a) but not large values (Figure 19d). The separation between the shoulder peaks is comparable to the line width for an absorption spectrum and increases as the line of sight approaches the cylinder axis due to the increase in the Doppler width. We stress that the typical radial column depth expected for an accretion column is $N_{e,21} \sim 10^3 - 10^4$, much larger than the value used in Figure 19. But we expect that, as the column depth of a cylindrical line-forming region increases, the properties of the emerging spectrum continue to be similar to those of a 1-1 line-forming region with $\Psi = \pi/2$, $\varphi_{sl} \sim 0$, and similar column depth. Specifically, the spectrum emerging from a cylindrical line-forming region with high N_e should possess a cyclotron line with large equivalent width at all viewing angles, and with no visible shoulders.

6. Implications for Accretion-Powered Pulsars and Gamma-Ray Bursters

Our understanding of how cyclotron line properties depend on geometry can provide important insights into the sources of observed cyclotron lines. It can shed light on the optical depth and location of the line-forming region in accretion powered pulsars; for example, whether line-formation occurs in the accretion column or in a thin scattering layer located in the pulsar magnetosphere. Understanding geometrical effects can also explain how cyclotron lines in gamma-ray bursts could be formed, e.g., by sources in a galactic corona.

6.1. Accretion-Powered Pulsars

Constructing fully self-consistent accretion-powered pulsar models that produce spectra in agreement with observation presents many challenges. These include determining what spectrum is appropriate for the injected photons, explaining why observed accretion-powered pulsar spectra contain an excess of photons at low energies compared with a Wien function, and reproducing the properties of the observed cyclotron features.

If the luminosity of the pulsar is small enough so that radiation forces are not important, the accreting material is stopped and the photons are produced at depths $N_{e,21} \sim 15,000 - 150,000$ ($\tau_T \sim 10 - 100$) beneath the stellar surface (Miller, Salpeter, and Wasserman 1987; Miller, Wasserman, and Salpeter 1989). Since the stopping depth is optically thick to (non-magnetic) Thomson scattering, many calculations assume a Wien spectrum at these depths. However, as we discussed in section 4.3, in a strong magnetic field the photons will not generally have a Wien distribution at these depths. Consequently, the injected spectrum needs to reflect the physics of the stopping process.

The $(E/E_B)^2$ dependence of the cross section for $E \ll E_B$ may play an important role in creating the photon excess at low energies. The excess in our own simulations is small compared with observations, but this is most likely due to our choice of a Wien distribution for the injected photons and our neglect of the velocity of the accreting material above the stopping depth.

Observed cyclotron features are broad, but shallow. For example, Soong *et al.* (1990) report a full-width half-maximum of 15.8 keV, but an equivalent width of only 10.3 keV for the line in the phase-averaged spectrum of Her X-1 (centroid at ~ 35 keV). In contrast, as we saw in Figure 18, theoretical calculations for line-forming regions with column depths typical of accretion columns ($N_{e,21} \sim 10^3 - 10^4$; Lamb, Pethick, and Pines 1973) generate lines which are extremely deep, with large equivalent widths. Similarly, in fits to the spectra of 4U 1538-52 and Vela X-1, Bulik *et al.* (1992, 1995) are unable to generate sufficiently broad lines in models with constant field strength. However, using a model with two field components, differing in strength by a factor ~ 5 , they obtain acceptable fits to the data. They suggest that scattering at the lower field component could correspond to scattering in a dipole field, $B(r) \sim B_o(R/r)^3$ at an altitude $r \gtrsim 0.3R$, where B_o is the surface dipole field strength and R is the stellar radius. The scattering could occur in an accretion mound, as in the model of Burnard, Arons, and Klein (1991), or in a suspended scattering atmosphere, as in the model of Dermer and Sturmer (1991) and Sturmer and Dermer (1994). Thus the spectrum could be the product of a combination of scattering near the surface and scattering in the magnetosphere.

The spectral signature of the geometry of the line-forming regions can provide insight into the contribution of each region to the spectrum. At moderate optical depths, spectra formed in the 1-1 geometry are characterized by prominent shoulders; these are smaller or absent in the 1-0. Although the prominence of the shoulders is a straightforward

consequence of scattering in a semi-infinite atmosphere, shoulders have not been reported in the observed spectra of accretion-powered pulsars. *If the shoulders persist after the model spectra have been folded through the detector response matrix, and they prevent an acceptable fit to an observed spectrum, their absence in the observed spectrum could be a significant clue to the geometry of the line-forming region* — it indicates either a geometry analogous to a 1-0 slab with no restriction on the column depth or a geometry analogous to a 1-1 slab with a column depth $N_{e,21} \gtrsim 15,000$ ($\tau_{T_o} \gtrsim 10$).

Using both 1-1 and cylindrical geometries, Araya and Harding (1996) consider the effects of line shoulders on the spectrum of the accretion-powered pulsar A0535+26. Kendziorra *et al.* (1992, 1994) report HEXE observations of 50 and 100 keV features from this pulsar at 2 and 4.5 σ respectively. OSSE observations by Grove *et al.* (1995) of a feature at 110 keV confirm the high energy feature reported by HEXE; the low energy feature is too close to the 45 keV OSSE threshold for a conclusive observation. Araya and Harding (1996) consider the possibility that the 110 keV feature is a second harmonic line in a spectrum where the first harmonic has been filled in by the line shoulders. They fit this model to the observed spectrum, for $N_{e,21} \lesssim 5$; the fit is poor compared with a model in which the 110 keV feature is the fundamental. The latter model is plausible in light of the low significance of the 50 keV feature in the HEXE observation.

Although the column depths in Araya and Harding’s (1996) calculation are suitable for scattering in the magnetosphere (see below), they are much smaller than the column depths usually considered typical of accretion columns. The results of section 5 in the present work, which show that the line shoulders disappear at large column depths, support the conclusion of Araya and Harding (1996) that A0535+26 does not possess a ~ 50 keV first harmonic line that has been filled in by the line shoulders. However, the spectrum of A0535+26 could possess a ~ 50 keV first harmonic that has been mostly filled in with

photons spawned by scattering at higher harmonics in a medium that is optically thick in the wings. It is difficult to assess this conjecture until second and higher harmonic scattering at such optical depths are better understood. In addition, the fact that the first harmonics observed in other accretion-powered pulsars are broad but shallow, with W_E much smaller than those given by theoretical models, gives pause.

In many accretion-powered pulsars, the pulse profiles are complex and strongly energy-dependent, and elude explanation by simple models. Dermer and Sturmer (1991) and Sturmer and Dermer (1994) suggest that some of these properties can be explained by photon scattering in the pulsar magnetosphere, in a layer of plasma supported by radiation pressure. Such an atmosphere has a geometry similar to the 1-0. By equating the momentum per second carried by the radiation to the gravitational force on the suspended plasma, Sturmer and Dermer calculate the *maximum* mass that can be suspended at a given altitude. At the maximum mass, these layers are optically thick to line scattering but thin to continuum scattering. They are located at a distance of a few stellar radii from the star's center. A calculation of the *actual* suspended mass needs to take into account the scattering cross section, the effects of multiple scatterings, and the stability of the suspended layer. We will address these issues in a separate paper.

Sturmer and Dermer calculate the effect of scattering in the suspended plasma on the radiation *pulse profiles*. They report that the scattering flattens the pulse profiles. The flattening corresponds to the reduction in flux at the line center that we see in our Monte Carlo spectra. In the present work we speculate about the signature of magnetospheric scattering on the *spectrum*. If a suspended layer could be formed, spectral features formed there would have small or no shoulders, in agreement with observations. At $\Psi = 0$, it would be difficult for a layer with $N_{e,21} \sim 1$ to form the broad lines required for the case of accretion-powered pulsars. However, as the present work shows, broad lines are not a

problem as Ψ approaches $\pi/2$. The lines would be broadened even more if the line-forming region covers an extended region in which the magnetic field strength varies significantly.

However, if the lines from an accretion-powered pulsar are formed in this way, one expects that the dipole field B_o at the neutron star surface would be ~ 10 times larger than the dipole component of the field $B(r)$ in the line-forming region in the magnetosphere. The field $B(r)$ can be inferred from the cyclotron line energy. For most sources, such as Her X-1, the field inferred from the cyclotron lines is *larger* than the dipole field inferred from the accretion torque model of Ghosh and Lamb (1979a,b; 1991), contrary to what would be expected if the lines are formed in the magnetosphere. However, it is possible that the *non-dipole* components of the field in the line-forming region is large enough to account for the discrepancy. There are also some accretion-powered pulsars in which the field inferred from the cyclotron line energy could conceivably be much *larger* than the dipole surface field inferred from the accretion torque theory (Ghosh and Lamb 1979a,b, 1991; Mihara 1995).

6.2. Gamma-ray Bursters

The fit to the spectrum of gamma-ray burst GB880205 made by Wang *et al.* (1989) assumes a static line-forming region with a uniform magnetic field parallel to the slab normal. As we mention in Section 1, this geometry is suitable, for example, for the magnetic polar cap of a neutron star with a dipole field. LWW point out that if the line-forming region is indeed at the polar cap, the static model is valid only if the bursters lie at distances less than several hundred parsecs. Otherwise, the burst luminosity exceeds the Eddington luminosity and the radiation force creates a relativistic plasma outflow along the field lines.

However, in order to explain the brightness and sky distributions of the burst observed by BATSE, it has been suggested that, if the bursters are galactic, the sources are in a

galactic corona at distances of 100-400 kpc (for a review, see Lamb 1995). In light of the BATSE results, it is important to explore line-formation models that are appropriate for sources at these distances.

One possibility is line-formation in a relativistic outflow (Miller *et al.* 1991, 1992; Isenberg, Lamb, and Wang 1996). Another possibility is line-formation in a static slab at the magnetic equator. Here the field lines are parallel to the slab ($\Psi = \pi/2$), and can confine the plasma magnetically (see, e.g., Zheleznyakov and Serber 1994, 1995). Using the revised Monte Carlo code developed in the present work, and varying Ψ , Freeman *et al.* (1996) fit models to the two observed spectra corresponding to the two time intervals S1 and S2 in which lines appeared in burst GB870303. When they perform a joint fit to the two intervals, using models with a common B_{12} and $N_{e,21}$ for both spectra but not a common viewing angle, they find that in the 1-1 geometry the data marginally favors the equatorial model over the polar model.

One promising line of future research is to calculate spectra for a region of a neutron star's surface large enough so that the field strength and orientation vary over the region. By comparing such calculations to observations, we can put a limit on how large a radiating area is compatible with the narrow lines found in gamma-ray bursts.

There are still many open issues concerning both models. For example, for the large magnetic fields and source distances required by the galactic corona model, the optical depths for the processes $\gamma \rightarrow e^+e^-$ and $\gamma\gamma \rightarrow e^+e^-$ are both much larger than unity (Schmidt 1978; Daugherty and Harding 1983; Burns and Harding 1984; Brainerd and Lamb 1987). The production of electron-positron pairs by these processes could lead to line-forming regions that are optically thick in the continuum, which might prevent the formation of the narrow lines observed in gamma-ray bursts. In addition, pair production could truncate the spectrum at the pair production threshold, 1 MeV. Truncation is

inconsistent with observations by COMPTEL (Winkler *et al.* 1993) and EGRET (Schneid *et al.* 1992; Kwok *et al.* 1993; Sommer *et al.* 1994) of photon energies up to 1 GeV with no evidence of a spectral cutoff or rollover at ≈ 1 MeV.

Various solutions to these problems have been proposed (for a review, see Higdon and Lingelfelter 1990). One possibility is that the entire spectrum is produced at the magnetic polar cap in a medium with bulk motion corresponding to a Lorentz factor of $\Gamma \sim 10$. The radiation would then be beamed into an angle $\sim 1/\Gamma$. For corona distances, the optical depth for the two photon process would then be reduced enough to be consistent with the observed spectra above 1 MeV (Schmidt 1978; Baring and Harding 1993; Harding and Baring 1994; Harding 1994). Additional calculations are necessary to determine whether the observed cyclotron features could be formed at the polar cap under these physical conditions.

Alternatively, the gamma-ray burst spectrum could consist of two components produced in two distinct physical regions: a soft ($\lesssim 1$ MeV) component produced in plasma trapped in the equatorial region of the magnetosphere (Lamb 1982; Katz 1982, 1994) and a hard component ($\gtrsim 1$ MeV) produced by relativistic outflow at the magnetic polar cap. Because the magnetic field traps the plasma in the line-forming region, the line-forming region can be static, even for highly super-Eddington luminosities, as is the case if the bursts come from neutron stars in a galactic corona. The hard component could be produced in a relativistic pair outflow or expanding fireball at the magnetic polar cap. If so, the cross section for the two photon process is further reduced by the bulk motion of the pairs. A recent report by Chernenko and Mitrofanov (1995) of evidence for two components in the spectrum of GB881024 is intriguing. The soft component dominates the spectrum for $E < 250$ keV; the hard component is dominant above this energy.

We wish to thank Tomasz Bulik, Deepto Chakrabarty, Peter Freeman, Cole Miller, and Rob Nelson for helpful discussions. This work was supported in part by NASA Grants NAGW-830, NAGW-1284, and NAG5-2868 at Chicago, and NASA Grant NAG5-3836 at Maryland. MI gratefully acknowledges the support of a NASA Graduate Student Researchers Fellowship under NASA Grant NGT-5-18.

A. Appendix – Calculation of T_c/E_B in Optically Thin Slabs

Start with eq. (16):

$$\Delta E \equiv \frac{\int d\Omega dE n(E, \Omega) \overline{\delta E} N_{scat}(\tau_{To}, E, \Omega)}{\int d\Omega dE n(E, \Omega)} , \quad (16)$$

In terms of the differential scattering cross section $d\sigma/d\Omega_s$,

$$\begin{aligned} \overline{\delta E} &\equiv \frac{\int dp f(p) d\Omega_s \frac{d\sigma}{d\Omega_s} \delta E}{\int dp f(p) d\Omega_s \frac{d\sigma}{d\Omega_s}} \\ &= \int dp d\Omega_s f(p) \frac{1}{\sigma_T \phi(E, \Omega)} \frac{d\sigma}{d\Omega_s} \delta E , \end{aligned} \quad (A1)$$

where $\delta E = E_s - E$ is the energy transferred from the electron to the photon in an individual scatter and ϕ is as defined in equation (14). Substituting eq. (A1) into (16) and adopting a normalized photon distribution, we obtain

$$\Delta E = \int d\Omega dE dp d\Omega_s n(E, \Omega) f(p) \frac{1}{\sigma_T \phi} \frac{d\sigma}{d\Omega_s} \delta E N_{scat}(\tau_{To}, E, \Omega) . \quad (A2)$$

In the optically thin, or single scattering limit, the total number of scatters per photon is just the fraction that experienced scattering, viz,

$$N_{scat}(\tau_{To}, E, \Omega) = 1 - \exp \left[-\frac{\tau(E, \Omega)}{|\mu_{sl}|} \right] \approx \frac{\tau}{|\mu_{sl}|}, \quad (\text{A3})$$

where for an isothermal medium

$$\frac{\tau}{|\mu_{sl}|} = \frac{\tau_{To} \phi(E, \Omega)}{|\mu_{sl}|} \ll 1, \quad (\text{A4})$$

is the depth at which photons are injected measured from the top of the slab, along the line of sight. Substituting eq. (A3) into (A2) gives

$$\Delta E = N_e \int_{-\infty}^{+\infty} dp f(p) \int \frac{d\Omega}{|\mu_{sl}|} dE n(E, \Omega) \left[\int d\Omega_s \frac{d\sigma}{d\Omega_s} E_s - E \int d\Omega_s \frac{d\sigma}{d\Omega_s} \right], \quad (\text{A5})$$

where we have used $\delta E = E_s - E$.

For first harmonic resonant scattering with zero natural line width, the differential cross section is given by eq. (10) in the limit $\Gamma_1 \rightarrow 0$ ($\hbar = c = k = 1$ used throughout):

$$\frac{d\sigma^r}{d\Omega_s^r} = \frac{9}{32} \frac{\sigma_T m_e}{\alpha} \delta(E^r - E_1^r) \frac{1 + \mu^{r2}}{2} \frac{1 + \mu_s^{r2}}{2}. \quad (\text{A6})$$

For atmospheres with $T_e \ll m_e$ and $b \ll 1$, the two naturally occurring small parameters are the electron velocity along the field [$\beta \sim (T_e/m_e)^{1/2}$] and the gyration velocity orthogonal to the field ($\beta_{gyr}^2 \sim b \sim E/m_e$). To evaluate T_c , we expand eq. (A5) to $O(\beta^2)$ and $O(b \sim E/m_e)$. Thus, the scattered frequency is given by $E_s = \gamma E_s^r (1 + \beta \mu_s^r)$, where

$$E_s^r = E^r \left\{ 1 - \frac{E^r}{2m_e} (\mu_s^r - \mu^r)^2 + O \left[\left(\frac{E^r}{2m_e} \right)^2 \right] \right\}. \quad (\text{A7})$$

We assume that the photon density is separable so that

$$n(E, \Omega) = n(E) Q(\Omega). \quad (\text{A8})$$

Substituting eqs. (12) and (A6)–(A8) into (A5), integrating over scattered angles, and integrating over E using

$$\delta(E^r - E_1^r) = \frac{1}{\gamma(1 - \beta\mu)} \delta(E - E_1), \quad (\text{A9})$$

where $E_1 = E_1^r / [\gamma(1 - \beta\mu)]$, gives

$$\begin{aligned} \Delta E \approx \frac{3\tau_{T_0} m_e}{16\pi\alpha} N_e \int_{-\infty}^{+\infty} dp f(p) \int \frac{d\Omega}{|\mu_{sl}|} Q(\Omega) N(E_1) E_1^r (1 + \mu^{r2}) \times \\ \left[1 - \frac{1}{\gamma^2(1 - \beta\mu)} - \frac{E_1^r}{m_e} \left(\frac{\mu^{r2}}{2} + \frac{1}{5} \right) \right]. \end{aligned} \quad (\text{A10})$$

The leading order term in brackets is $O(\beta)$ and so we need only expand $N(E_1)E_1^r(1 + \mu^{r2})$ to $O(\beta)$ to obtain the desired result. Doing this gives

$$\begin{aligned} \Delta E = \frac{3\tau_{T_0} m_e}{16\pi\alpha} N(E_B) E_B \int_{-\infty}^{+\infty} dp f(p) \int \frac{d\Omega}{|\mu_{sl}|} Q(\Omega) \times \\ \left\{ -\beta\mu(1 + \mu^2) + \beta^2[1 + (s + 2)\mu^2 + (s - 3)\mu^4] - b(1 + \mu^2) \left(\frac{\mu^2}{2} + \frac{1}{5} \right) \right. \\ \left. + O(\beta^3, b\beta) \right\}, \end{aligned} \quad (\text{A11})$$

where

$$s \equiv - \frac{E}{n(E)} \frac{dn}{dE} \Big|_{E=E_B}. \quad (\text{A12})$$

Note that if the initial photon spectrum is a power law, $n(E) \propto E^{-\alpha}$, then s is just the spectral index, α .

We assume $f(p)$ to be a non-relativistic one-dimensional Maxwellian, that is,

$$f(p) dp = \frac{\exp\left(\frac{-p^2}{2m_e T_e}\right)}{\sqrt{2\pi m_e T_e}} dp . \quad (\text{A13})$$

Integrating over p in eq. (A11) and setting $\Delta E = 0$ gives the slab Compton temperature

$$\frac{T_c}{E_B} = \frac{1}{10} \frac{\int \frac{d\Omega}{|\mu_{sl}|} Q(\Omega) (2 + 7\mu^2 + 5\mu^4)}{\int \frac{d\Omega}{|\mu_{sl}|} Q(\Omega) [1 + (s + 2)\mu^2 + (s - 3)\mu^4]} . \quad (\text{A14})$$

REFERENCES

- Adams, T. F. 1972, *ApJ*, 174, 439.
- Adler, S. L. 1971, *Ann. Phys.*, 67, 599.
- Araya, R.A., and Harding, A.K. 1996, *ApJ*, 463, L33.
- Alexander, S.G., and Mészáros, P. 1989, *ApJ*, 344, L1.
- Baring, M. G. and Harding, A. K. 1993, in *Proc. 23rd ICRC*, 1, 53.
- Briggs, M.S. 1996, in *AIP Conf. Proc. No. 384, Gamma-Ray Bursts, 3rd Huntsville Symposium*, ed. C. Kouveliotou, M. Briggs, and J. Fishman (New York: AIP), 133.
- Bulik, T. 1993, Ph.D. Thesis, Pennsylvania State University.
- Bulik, T. *et al.* 1992, *ApJ*, 395, 564.
- Bulik, T. *et al.* 1995, *ApJ*, 444, 405.
- Brainerd, J.J. and Lamb, D.Q. 1987, *ApJ*, 313, 231.
- Burnard, D.J., Arons, J., and Klein, R.I. 1991, *ApJ*, 367, 575.
- Burns, M.L. and Harding, A.K. 1984, *ApJ*, 285, 747.
- Canuto, V., Lodenguai, J., and Ruderman, M. A. 1971, *Phys. Rev. D*3, 2303.
- Chandrasekhar, S. 1960, *Radiative Transfer* (New York: Dover Publications, Inc.).
- Chernenko, A. and Mitrofanov, I. 1995, *MNRAS*, 274, 361.
- Clark, G.W. *et al.* 1990, *ApJ*, 353, 274.
- Daugherty, J.K. and Harding, A.K. 1983, *ApJ*, 273, 761.

- Daugherty, J. K. and Ventura, J. 1977, *A&A*, 61, 723.
- Daugherty, J. K. and Ventura, J. 1978, *Phys. Rev. D*, 18, 1053.
- Dermer, C.D. and Sturmer, S.J. 1991, *ApJ*, 382, L23.
- Fenimore, E.E. *et al.* 1988, *ApJ*, 335, L71.
- Freeman, P.E. *et al.* 1992 in *AIP Conf. Proc. No. 265, Gamma Ray Bursts*, ed. W.S. Paciesas and G.J. Fishman (New York: AIP), 216.
- Freeman, P.E. *et al.* 1996 in *AIP Conf. Proc. No. 366, High Velocity Neutron Stars and Gamma-ray Bursts*, ed. R.E. Rothschild and R.E. Lingenfelter (New York: AIP), 211.
- Ghosh, P. and Lamb, F.K. 1979a, *ApJ*, 232, 259.
- Ghosh, P. and Lamb, F.K. 1979b, *ApJ*, 234, 296.
- Ghosh, P. and Lamb, F.K. 1991 in *Neutron Stars: Theory and Observations*, ed. J. Ventura and D. Pines (Dordrecht: Kluwer Academic Publishers), 363.
- Graziani, C. 1993, *ApJ*, 412, 351.
- Grove, J. E. *et al.* 1995, *ApJ*, 438, L25.
- Harding, A. K. 1994, in *AIP Conf. Proc. No.304, The Second Compton Symposium*, ed. C. Fichtel, N. Gehrels, J.P. Norris (New York: AIP), 30.
- Harding, A. K. and Baring, M. G. 1994, in *AIP Conf. Proc. No. 307, Gamma-Ray Bursts*, ed. G. Fishman, J.J. Brainerd, and K. Hurley, (New York:AIP) 520.
- Harding, A.K. and Daugherty, J.K. 1991, *ApJ*, 374, 687.
- Harding, A.K., and Preece, R.D. 1989, *ApJ*, 338, L21.

Herold, H. 1979, *Phys. Rev. D*19, 2868.

Heuter, G.J. 1984, in *AIP Conf. Proc. No.77, Gamma-Ray Transients and Related Astrophysical Phenomena*, ed. R.E. Lingenfelter, H.S. Hudson, and D.M. Worrall (New York: AIP), 189.

Higdon, J.C. and Lingenfelter, R.E. 1990, *ARA&A*, 28, 401.

Isenberg, M., Lamb, D.Q., and Wang, J.C.L. 1996, in *AIP Conf. Proc. No. 384, Gamma-Ray Bursts, 3rd Huntsville Symposium*, ed. C. Kouveliotou, M. Briggs, and J. Fishman (New York: AIP), p. 187.

Kaminker, A.D., Pavlov, G.G., and Shibano, Y.A. 1982, *Ap&SS*, 86, 249.

Kaminker, A.D., Pavlov, G.G., and Shibano, Y.A. 1982, *Ap&SS*, 91, 167.

Katz, J. 1982, *ApJ*, 260, 371.

Katz, J. 1994, *ApJ*, 422, 248.

Kendziorra, E. *et al.* 1992, in *Proc. 28th Yamada Conference, Frontiers of X-Ray Astronomy*, ed. Y. Tanaka and K. Koyama (Tokyo: Univ. Acad.), 51.

Kendziorra, E. *et al.* 1994, *A&A*, 291, L31.

Kwok, P.W. *et al.* 1993, in *Proc. Compton Symposium*, ed. N. Gehrels (New York: AIP), 855.

Lamb, D.Q. 1982, *Ann. N.Y. Acad. Sci.*, 422, 237.

Lamb, D.Q. *et al.* 1989, in *Proc. 14th Texas Symp. on Relativistic Astrophysics*, ed. E. Fenyves (New York:Ann. NY Acad Sci.), 571, 460.

Lamb, D.Q. 1995, *PASP*, 107, 1152.

- Lamb, D.Q., Miller, M.C., and Taam, R.E., 1996, Los Alamos E-Print Archive, astro-ph/9604089.
- Lamb, D.Q., Wang, J.C.L., and Wasserman, I.M. 1990, ApJ, 363, 670.
- Lamb, F.K., Pethick, C.J., and Pines, D. 1973, ApJ, 184, 271.
- Makishima, K. and Mihara, T. 1992, in *Frontiers of X-Ray Astronomy*, Y. Tanaka and K. Koyama, eds., (Tokyo: Universal Academy Press), p. 23.
- Mazets, E.P. *et al.* 1980, AZh. Pis'ma, 6, 706.
- Mazets, E.P. *et al.* 1981, Nature, 290, 378.
- Mazets, E.P. *et al.* 1996, in *AIP Conf. Proc. No. 384, Gamma-Ray Bursts, 3rd Huntsville Symposium*, ed. C. Kouveliotou, M. Briggs, and J. Fishman (New York: AIP), p. 492.
- Mészáros, P. and Nagel, W. 1985, ApJ, 298, 147.
- Mihara, T. 1995, Ph.D. Thesis, University of Tokyo.
- Miller, G.S., Salpeter, E.E., and Wasserman, I. 1987, ApJ, 314, 215.
- Miller, G.S., Wasserman, I., and Salpeter, E.E., 1989, ApJ, 346, 405.
- Miller, G.S. *et al.* 1991, Phys. Rev. Lett., 66, 1395.
- Miller, G.S. *et al.* 1992, in *Gamma-ray Bursts: Observations, Analyses, and Theories*, Cheng Ho, R.I. Epstein, and E.E. Fenimore, eds., (Cambridge: Cambridge University Press), p. 215.
- Murakami, T. *et al.* 1988, Nature, 335, 234.
- Nagel, W. 1981, ApJ, 251, 288.

- Nelson, R. W., Salpeter, E. E., and Wasserman, I. 1993, *ApJ*, 418, 874.
- Nelson, R. W. *et al.* 1997, *Astron. Soc. Pac. Conf. Ser.*, in press.
- Nishimura, O. 1994, *PASJ*, 46, 45.
- Nishimura, O. and Ebisuzaki, T. 1992, *PASJ*, 44, 109.
- Osterbrock, D. E., 1962, *ApJ*, 135, 195.
- Ruderman, M., 1991a, *ApJ*, 366, 261.
- Ruderman, M., 1991b, *ApJ*, 382, 576.
- Ruderman, M., 1991c, *ApJ*, 382, 587.
- Rybicki, G.B. and Lightman, A.P. 1979, *Radiative Processes in Astrophysics* (New York: John Wiley and Sons).
- Schmidt, W.K.H. 1978, *Nature*, 271, 525.
- Schneid, E. *et al.* 1992, *A&A*, 255, L13.
- Slater, G., Salpeter, E.E., and Wasserman, I.M. 1982, *ApJ*, 255, 293.
- Sommer, M. *et al.* 1994, *ApJ*, 422, L63.
- Soong, Y. *et al.* 1990, *ApJ*, 348, 641.
- Sturmer, S.J. and Dermer, C.D. 1994, *Astron. and Astrophys.*, 284, 161.
- Trümper, J. *et al.* 1978, *ApJ*, 219, L105.
- Ventura, J. 1979, *Phys. Rev. D*19, 1684.
- Wang, J.C.L., Wasserman, I.M., and Salpeter, E.E. 1988, *ApJS*, 68, 735.

Wang, J.C.L., Wasserman, I.M., and Salpeter, E.E. 1989, ApJ, 338, 343.

Wang, J.C.L. *et al.* 1989, Phys. Rev. Lett., 63, 1550.

Wang, J.C.L., Wasserman, I., and Lamb, D.Q., 1993, ApJ, 414, 815.

Wasserman, I. and Salpeter, E. E. 1980, ApJ, 241, 1107.

Wheaton, W.A. *et al.* 1979, Nature, 282, 240.

Winkler, C. *et al.* 1993, in *Proc. Compton Symposium*, ed. N. Gehrels (New York: AIP),
845.

Yoshida, A. *et al.* 1991, PASJ, 43, L69.

Zheleznyakov, V. V. and Serber, A. V. 1994, Sp. Sci. Rev., 68, 275.

Zheleznyakov, V. V. and Serber, A. V. 1995, Adv. Sp. Res., vol 16, no. 3, pg. 77.

Fig. 1.— Line-forming region geometries. (a) Slab geometry with magnetic field direction at an angle Ψ to the slab normal. The slab is infinite in extent. N_e is the column depth between the source plane and the top surface; N'_e is the column depth between the bottom surface and the source plane. θ_{sl} and φ_{sl} denote the polar and azimuthal angles of the photon direction with respect to the slab normal respectively. (b) Cylindrical geometry with magnetic field parallel to cylinder axis. The cylinder is infinite in length. N_e is the column depth between the photon source, located along the cylinder axis, and the surface. In both geometries, θ is the angle between the photon direction and the magnetic field direction.

Fig. 2.— Scattering profiles vs. photon energy for field strength $B_{12} = 3.5$ ($E_B = 40$ keV), $T_e = 10$ keV, and incident photon direction cosine $\mu = 0, 0.5,$ and 1 . Panels (a)–(c) ϕ_0 (*dots*), ϕ_1 (*dashes*), and $\phi_0 + \phi_1$ (*solid*), including non-Lorentzian factor $4E^{r3}E_B^{-1}(E^r + E_B)^{-2}$. Panels (d)–(f) Comparison of $\phi_0 + \phi_1$ with (*solid*) and without (*dot-dash*) non-Lorentzian factor.

Fig. 3.— Resonant Compton temperature T_c/E_B as a function of the angle Ψ between the magnetic field and the slab normal for optically thin models ($\tau/|\mu_{sl}| \ll 1$) with $B_{12} = 1.7$, first harmonic scattering only, and zero natural line width. The *solid curve* is the analytic result with non-relativistic scattering kinematics. Monte Carlo calculations using the 1-1 line-forming region geometry are shown for non-relativistic kinematics (*squares*), relativistic kinematics with both p_{max} and p_{min} channels open (*triangles*), and relativistic kinematics with only the p_{min} channel open (*circles*).

Fig. 4.— Monte Carlo calculations of the equilibrium Compton temperature T_c/E_B as a function of the angle Ψ between the magnetic field and the slab normal for slabs that are optically thick in the line core. The calculations use $N_{e,21} = 1.2$ and $B_{12}=1.7$. Temperatures are shown for line-forming regions with both the 1-0 (*circles*) and 1-1 (*triangles*) geometries.

Fig. 5.— The mean energy associated with the net photon flux as a function of depth inside a slab with field strength $B_{12} = 3.5$, field orientation $\Psi = 0$, and column depth $N_{e,21} = 15,000$ ($\tau_{T_o} = 10$). The source plane is at $\tau_T/\tau_{T_o} = 1$ and the upper surface is at $\tau_T/\tau_{T_o} = 0$. Results for the 1-1 (*solid*) and 1-0 (*dashes*) geometries are shown. The mean energy at the source plane in the 1-1 geometry is zero because of the net zero flux at this location.

Fig. 6.— Cumulative injected (*dots*) and emerging (*solid*) spectra for a slab with field strength $B_{12} = 3.5$, field orientation $\Psi = 0$, and column depth $N_{e,21} = 15,000$ ($\tau_{T_o} = 10$). The injected spectra is a 10 keV Wien distribution. Even though only 14% of the photons are injected with $E < E_{\text{thin}}(7) = 12.9$ keV (*dashes*), 45% escape below this energy. The glitch in the emerging spectrum just above $E_{\text{thin}}(7)$ is due to the random fluctuations in the Monte Carlo simulation. The output bin for this energy holds an unusually low number of photons.

Fig. 7.— Spectra for $\Psi = 0$ and several viewing angles. $B_{12}=1.7$ and $N_{e,21}=1.2$. Monte Carlo spectra for the 1-1 (*solid*) and 1-0 (*dots*) geometries are shown, as well as relativistic absorption spectra with finite natural line width (*dashes*).

Fig. 8.— Spectra for $\Psi = \pi/4$ and several viewing angles. $B_{12}=1.7$ and $N_{e,21}=1.2$. Monte Carlo spectra for the 1-1 (*solid*) and 1-0 (*dots*) geometries are shown, as well as relativistic absorption spectra with finite natural line width (*dashes*).

Fig. 9.— Spectra for $\Psi = \pi/2$ and several viewing angles. $B_{12}=1.7$ and $N_{e,21}=1.2$. Monte Carlo spectra for the 1-1 (*solid*) and 1-0 (*dots*) geometries are shown, as well as relativistic absorption spectra with finite natural line width (*dashes*).

Fig. 10.— Equivalent width of the first harmonic line as a function of viewing angle in the 1-0 geometry. The calculations use $B_{12}=1.7$, $N_{e,21}=1.2$, $T_c=8.38$ keV, and $\Psi = \pi/4$. The equivalent widths become negative (i.e., there are emission-like features) as μ_{sl} approaches unity. The surface is symmetric about $\varphi_{sl} = \pi/2$.

Fig. 11.— Equivalent width of the first harmonic line as a function of viewing angle in the 1-1 geometry. The calculations use $B_{12}=1.7$, $N_{e,21}=1.2$, $T_c=9.76$ keV, and $\Psi = \pi/2$. The equivalent widths become negative (i.e., there are emission-like features) as μ_{sl} approaches unity. The surface is symmetric about $\varphi_{sl} = \pi/2$.

Fig. 12.— First harmonic equivalent width as a function of μ_{sl} for the 1-0 (*dashes*) and 1-1 (*solid*) geometries for different values of Ψ and $N_{e,21}$. $B_{12}=1.7$.

Fig. 13.— Angular distribution of emerging radiation for isotropic photon injection at $E = E_B$, $B_{12} = 1.7$ and $N_{e,21} = 1.2$. The spectrum $N(\mu_{sl})$ is summed over energies and averaged over the azimuthal angle φ_{sl} . In the 1-0 geometry, the angular distributions of both the transmitted (*solid*) and reflected (*dashes*) spectra are shown. In the 1-1 geometry the transmitted and reflected spectra are identical, by symmetry. The distributions are normalized so that the sum of the transmitted and reflected spectra is equal to unity. The photons tend to escape transverse to the slab, regardless of the direction of the magnetic field.

Fig. 14.— Shoulder formation for $\Psi = 0$. Spectra for absorption (*dashes*) and scattering (*dots*) from the first harmonic only are shown. When higher harmonics (and spawning) are included (*solid*), the shoulders are enhanced.

Fig. 15.— Shoulder formation for $\Psi = \pi/2$. Spectra for absorption (*dashes*) and scattering (*dots*) from the first harmonic only are shown. When higher harmonics (and spawning) are included (*solid*), the shoulders are enhanced.

Fig. 16.— Angle-integrated energy spectra for 1-1 atmospheres with $B_{12} = 1.7$, $N_{e,21} = 1.2$, $T_e = T_c - 2$ keV (a,b), T_c (c,d), and $T_c + 2$ (e,f), and for both $\Psi = 0$ and $\Psi = \pi/2$. For $T_e < T_c$, the majority of the scattered power escapes the atmosphere in the red line shoulder. For $T_e > T_c$, the majority of the scattered power escapes in the blue line shoulder.

Fig. 17.— Angle-integrated flux of photons with $\mu_{sl} > 0$ at four points inside the slab for field strength $B_{12} = 1.7$, field orientation $\Psi = 0$, and column depth $N_{e,21} = 1.2$. The flux is shown for the 1-1 (*solid*) and 1-0 (*dots*) geometries. The source plane is at $\tau_T/\tau_{T_o} = 1$ and the upper surface is at $\tau_T/\tau_{T_o} = 0$.

Fig. 18.— Angle-integrated flux of photons with $\mu_{sl} > 0$ at several points inside the slab for field strength $B_{12} = 3.5$, field orientation $\Psi = 0$, column depths $N_{e,21} = 30$ ($\tau_{T_o} = 0.02$), 1,500 ($\tau_{T_o} = 1$), and 15,000 ($\tau_{T_o} = 10$), and a Wien injected spectrum with $kT_\gamma = kT_e = 10$ keV. The flux is shown for the 1-1 (*solid*) and 1-0 (*dots*) geometries. The cyclotron energy is indicated by the vertical dashed line.

Fig. 19.— Spectra for cylindrical line-forming region with magnetic field $B_{12}=1.7$ oriented along the cylinder axis. The column density from the cylinder axis to the surface is $N_{e,21} = 1.2$. The viewing angle is characterized by $\mu = \cos \theta$ where θ is the angle between the magnetic field and the line of sight. Monte Carlo spectra for scattering (*solid*) and absorption (*dashes*) are shown.

Table 1. Dependence of resonant Compton temperature on orientation of the magnetic field, higher harmonics, and natural line width

Channels open	Natural line width	T_c/E_B ($\Psi = 0$)	T_c/E_B ($\Psi = \pi/2$)
1-0 Geometry			
first three harmonics	finite	$0.299^{+0.005}_{-0.004}$	$0.425^{+0.007}_{-0.008}$
0 \rightarrow 1 \rightarrow 0 only	finite	$0.274^{+0.005}_{-0.005}$	$0.350^{+0.010}_{-0.012}$
0 \rightarrow 1 \rightarrow 0 only	zero	$0.262^{+0.005}_{-0.005}$	$0.352^{+0.009}_{-0.009}$
1-1 Geometry			
first three harmonics	finite	$0.357^{+0.003}_{-0.003}$	$0.495^{+0.006}_{-0.006}$
0 \rightarrow 1 \rightarrow 0 only	finite	$0.363^{+0.003}_{-0.004}$	$0.469^{+0.008}_{-0.007}$
0 \rightarrow 1 \rightarrow 0 only	zero	$0.361^{+0.004}_{-0.004}$	$0.514^{+0.010}_{-0.009}$

Note. — Compton temperatures are for $B_{12} = 1.7$ and $N_{e,21} = 1.2$. The effect of the higher harmonics and natural line width is small. The quoted errors are statistical.

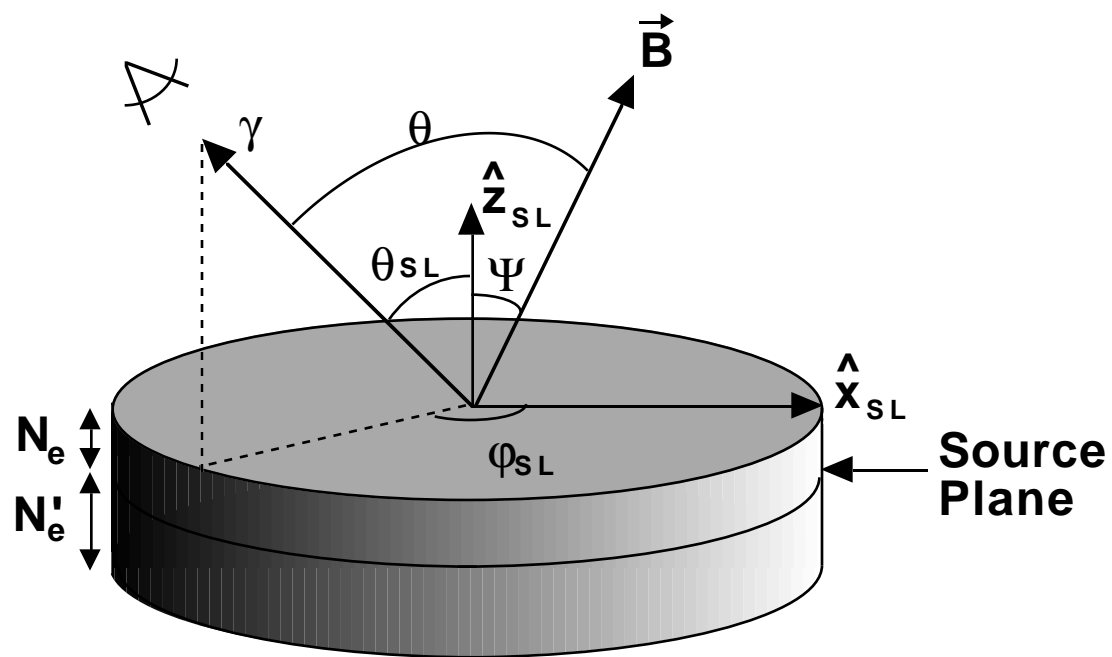
Table 2. Large optical depth simulations. For all simulations, $B_{12} = 3.5$, $\Psi = 0$, and the injected photons have a Wien distribution with temperature $T_\gamma = T_e = 10$ keV.

$N_{e,21}$	0 \rightarrow 0 channel		τ_1	$a\tau_1$	N_{scat}^a	$\langle E_t(\tau_T = 0) \rangle$ (keV)
	open	τ_{To}				
1-0 Geometry						
30	Yes	0.02	280	0.56	39	26.2
1,500	Yes	1	14,000	28	3,280	19.3
15,000	Yes	10	140,000	280	64,000	14.3
1-1 Geometry						
30	Yes	0.02	280	0.56	435	28.8
1,500	Yes	1	14,000	28	22,300	24.6
1,500	No	1	14,000	28	20,800	24.9
15,000	Yes	10	140,000	280	233,000	15.5
15,000 ^b	Yes	10	140,000	280	806,000	24.7
15,000	No	10	140,000	280	173,000	16.4
150,000	Yes	100	1,400,000	2,800	5,560,000	10.6
150,000	No	100	1,400,000	2,800	1,080,000	9.3

^aNumber of scatterings per transmitted photon

^bCross section does not include non-Lorentzian factor

(a)



(b)

